공학박사학위논문

Brain-on-a-Chip:
Neural Circuit and Blood-Brain Barrier on Microfluidic Platform

미세 유체 소자 내 신경 회로와 혈액-뇌 장벽 모사를 통한 브레인-온-어-칩 개발

2018 년 2 월

서울대학교 대학원

기계항공공학부

방 석 영

Abstract

In this thesis, we aim to mimic complex brain tissue in various ways on a microfluidic platform. The brain tissue is so complex that it is still not fully known. The human brain consists of about 100 billion neurons and 10 times more glial cells such as astrocytes, oligodendrocytes, and microglia. The various and numerous cells present in the brain are not randomly arranged but form delicate and complex structures. Two representative structures of the complex brain are the neural circuits and the blood-brain barrier. The characteristic of the neural circuit is that signals are unidirectionally transmitted by the axons aligned in one direction. The feature of the blood-brain barrier is that astrocytes, one type of glia cells, contact the blood vessels and reduce blood vessel permeability. Conventional *in vitro* cell cultures are made in a simple 2D environment such as a petri dish or a cover slip, which is very different from the *in vivo* brain environment. In order to overcome these limitations, it is necessary to use a microfluidic platform for the control the cell size level channel design, the structural modification of the hydrogel using pressure, and the channel design for two or more cell co-culture.

First, we study the effect of the shape of the channel at the cell size level on the axon growth of neurons. Neurons receive signals from a number of short dendrites and deliver them to one long axon to transmit signals. In order to investigate the growth characteristics of long and thin axons, microchannels which can only pass through the axons of the neurons were prepared. The design of the microchannel is designed to determine in which direction the axon grows by a straight line after a specific length of growth. As a result, it is confirmed that the axon protrudes more than 120 μm and grows straightly in the corresponding direction in the subsequent growth. Using these axonal growth characteristics, we design a repeating microchannel with a ring shape. As a result, it is confirmed that a unidirectional neural circuit is formed in which axonal protrusions are connected in only one direction between two separated groups of neurons.

Next, we study the effect of this hydrogel on axon growth after changing the pattern of internal density with the pressure of a patterned hydrogel on a microfluidic platform. Matrigel, a type of ECM hydrogel, is patterned on a microfluidic platform designed by arranging three arrays of micro-posts which have 100 μm size with spaced 100 μm apart. Thereafter, a water pressure of about 12 mm is applied only to one side of the Matrigel through

the media channel. When this asymmetric pressure is applied for more than 3 hours, the Matrigel is pushed out between the micro-posts. The same amount of cell culture medium is then placed on both sides of the Matrigel to stabilize the Matrigel in a deformed state. As a result, the internal density of the deformed Matrigel is anisotropic and the internal density is patterned regularly in the dense region and in the sparse region. When the neurons are attached to one side of the deformed Matrigel, the axon protrusions of the neurons gathere at the sparse density of the Matrigel to form bundle shape. These bundle-shaped axon assemblies are also observed in neural circuits of the *in vivo* brain. By modifying the design of the microfluidic platform, another neuron group is placed at the end of the axon bundles, and it is confirmed that an *in vitro* 3D neural circuit similar to that of the neural circuit of the brain is structurally and functionally constructed.

Finally, we study the effect of co-culture method which can provide cell culture medium suitable for more than two cells co-cultured in microfluidic platform. In order to establish co-culture condition of endothelial cells and neural cells, culture is started stably only with endothelial cells rather than growing both cells from the beginning. At this time, only endothelial cell culture medium is used. The neural cells are attached to one side of the

hydrogel as the endothelial cells begin to form a vascular network inside the patterned hydrogel between the two cell culture channels on the microfluidic platform. From this point on, neuron culture medium is used for the neural cell side channel and endothelial cell culture medium is used for the opposite channel. After 5 days or more, the lumen of the vascular network is opened only to the channel of the endothelial cell culture medium. That is, endothelial cell culture medium is provided inside the vascular network, and neuron culture medium is provided independently as the neural cell. As a result of cell culture under this co-culture conditions it is confirmed that both morphological characteristic such as astrocytes contacting blood vessels and functional characteristic such as low permeability of blood vessels is formed which are seen in the blood-brain barrier of *in vivo* brain tissue.

As shown in the above results, the neurons are sensitive to the microchannel shape or deformed hydrogel on the microfluidic platform. We can use these physical or mechanical elements to control the growth pattern of neurons. In addition, we have developed a method to provide a cell culture condition suitable for each cell type for co-culture of various cells. A brain-on-a-chip formed using a microfluidic platform capable of precisely controlling the structure and function of neural cells can be applied to various

fields such as a platform for basic neuroscience research and high-throughput drug screening.

Key Words: Microfluidic platform, Neural cell, Neural circuit, Axon diode, Axon bundle, Blood-brain barrier, Cell co-culture

Student Number: 2012-22556

Contents

List of Tables

List of Figures

on the figure. (C) Quantification showed that 83.40 ± 13.35% of axons grew straight (within a range of ± 15° from the center line).

Figure 2-4. Growth cone behavior for maintaining directionality. (A) Schematic of the microstructure comprising two forked channels. When an axon grew out through the microchannel (distance L), it could extend in a new direction (channel 1) or maintain its original direction (channel 2). (B) Fluorescence image of a microfluidic culture to observe maintaining axon growth direction after being turned physically. The microchannel length, from the direction change point to the forked point, was in the range of 30 to 240 μm. (C) Quantification showed that the number of axons growing in the new direction (channel 1) increased significantly as distance L increased. In particular, most axons extended in the new direction (channel 1) when the distance L was more than 120 μm.

Figure 2-5. In vitro neural network using the "neural diode" in a microfluidic culture device. Design of the forward bias (A) and backward bias (B) neural diode. They are magnified image of C, D. Channel 1 and 2 are seeded with neurons simultaneously and co-stained green/red at 14 DIV. The length of a point to b point is more than 120 μm for retained axon directionality. Fluorescence image of the presynaptic channel 1 and postsynaptic channel 2 in microfluidic cultures. (C) Axons in the presynaptic channel 1 reached the opposite side. (D) However, axons in the postsynaptic channel 2 could not reach the opposite channel 1 due to the effect of the diode repeated three times. (E) Quantification showed that the neural diodes efficiently polarize axonal growth. An axon extending with forward bias could readily pass the diode. (F) However, an axon extending with backward bias could not reach the opposite channel within the second diode. (G) When lower cell density is used (less than 6×10^6 cells ml^{-1}), cell viability is adversely affected. For higher cell densities up to 10×10^6 cells ml^{-1} resulted

in similar high selectivity of the diode.

Figure 2-6. To observe clearly whether an axon reached opposite channels, we made a mask of axon distribution based on fluorescence images. (A) Neurons in presynaptic channel 1 could easily extend to postsynaptic channel 2. (B) However, neurons in postsynaptic channel 2 could not reach the presynaptic channel 1 after three times of repeated neuron diode.

Figure 2-7. (A) Image of the whole neural diode device (red: forward bias, green: backward bias). (B) Schematic images for the experimental protocol (microfluidic neural diode: normal direction) used in C–E. (C) Representative time-lapse images for the Fluo-4-AM Ca^{2+} response before and after a brief (2-second) treatment with 90 mM high KCl on the other side of the microfluidic channels. (D, E) Representative 3D plot for the Ca^{2+} response. Red boxes indicate the time points above arbitrary threshold (fluorescence increased more than 50% versus the initial fluorescence). (F) Schematic images for the inverse experimental protocol (microfluidic neural diode: reverse direction) used in G–I. (G) Representative time-lapse images for the Fluo-4-AM Ca^{2+} response before and after treatment with 90 mM high KCl on the other side of the microfluidics. (H–I) Representative 3D plot for the Ca^{2+} response. Note that there are no activated neurons by 90 mM high KCl, treated on the other side of the microfluidics. Small and unsynchronized Ca^{2+} peak showed spontaneous activity of neurons. (J) Statistical analysis for B–I. In the forward bias stimulation, we measured decay time constant (τ) for Ca^{2+} clearance (4.67 ± 0.48 seconds). (K) Successive Ca^{2+} responses during multiple treatments with 90 mM high KCl. Presynaptic neurons were stimulated with a three consecutive 5-second treatment with high KCl, each followed by 45 seconds of resting period.

Figure 3-1. Three-dimensional (3D) neurite bundle formation in ECM hydrogel. (A) Structural feature of the neural circuit in the brain. A group of neurons form fasciculated bundles to reach its target post-synaptic cells. (B) Photograph of the 3D neural circuit device. (C) (i) Schematic of microfluidic device (box, SEM image of micro-pillar array. Scale bar, 200 μm), (ii) Gel loading step, (iii) 3D Matrigel alignment during gelation using hydrostatic pressure, (iv) Neuron plating step, and (v) Neurite bundle formation along flow direction in 3D Matrigel.

Figure 3-2. Comparison between random and deformed gel Matrigel. Collagen type IV, which is one of the main components in Matrigel, is visualized by anti-collagen immunostaining. Neurons are attached on the left side of the Matrigel. The red arrow indicates the direction of neurite propagation. A) (i) Randomly cross-linked Matrigel, Collagen type IV density distribution is evenly situated between micro-pillar arrays. (ii and iii) Neurites are spread through all directions including z-axis. B) Deformed Matrigel. Hydrostatic pressure was applied on the left side of device. (i) Collagen type IV distribution is deformed between micro-pillar arrays. (ii and iii) The scale bar indicates 200 μm (i-iii) and 100 μm (dashed box).

Figure 3-3. Quantification of neurite bundle formation as a function of various design parameters. A) We quantified the neurite bundle length based on the difference of the number of channels and the channel width. The total width of the ECM channel for all cases was maintained at a constant value of 1500 μm. The bundle width was measured at the dashed line position. (i) Axon formation was visualized by Calcein AM staining. For a device with single, double, and triple gel channels, the axon bundles had (ii) longer and (iii) more slender characteristics as the gel channel number increased. B) We quantified the neurite bundle formation with various micro-pillar gap sizes. (i) Images of neurite bundles shape with difference gap size. Increasing the gap

size leads to (ii) a decrease in axon bundle length, and (iii) an increase in axon bundle width. The scale bar indicates 200 μm. Red arrow in the color map image indicates the direction of neurite bundle propagation.

Figure 3-4. We introduced circular arc shape ECM hydrogel channels. After applying hydrostatic pressure, axon bundles grew in radial direction.

Figure 3-5. Characteristics of the bundle formation platform. A) Optimization of plated neuronal cell density. Fluorescence images of axons stained with calcein AM at 15 DIV. The plating concentration was optimized at 6×10^6 cells mL^{-1} as compared to other different concentration values. (i and ii) Cell density of less than 6×10^6 mL^{-1} did not have the capability of extending axons at long distances and maintaining neurite alignment as well as forming axon bundles. (iv) In contrast, axon fasciculations were dispersed at cell concentrations higher than 6×10^6 cells mL^{-1}. B) Optimization of neurites growth period. (i-iii) Neurites from the plated neurons were able to extend more than 1500 μm and axon fasciculation was formed after 6 days in vitro. (iv) Neurites grew into the deformed Matrigel at the average speed of 250 μm day^{-1} until 4 DIV. At 6 DIV, most neurites reached the opposite end of Matrigel (B. iv). (Scale bar: 200 μm.)

Figure 3-6. Three-dimensional neural circuit construction with fasciculate bundles. A) Schematic of aligned 3D neural circuit device. Pre-synaptic and post-synaptic neuron groups generated neural networks parallel with the deformed ECM components. B) Neural circuit composed of pre-synaptic neuron group, neurite bundle region, and post-synaptic neuron group. The neural circuit was visualized with calcein AM and Hoechst. C) Synapses at post-synaptic neuron group area. Neuronal cells were immunostained with a pre-synaptic marker (synaptophysin, red) and post-synaptic marker (PSD95,

green) at 12 DIV. (ii)Synapses were detected by fluorescence imaging with pre-synaptic and post-synaptic marker signals being adjacent to one another. D) Intracellular calcium live imaging of a three-dimensional neuronal circuit. (i) Fluorescence image of BAPTA-1 AM-loaded 3D neuronal network at 14 DIV. Numbers indicate the change point of fluorescent intensity. (ii) The fluorescent intensity represents the intracellular calcium ion concentration. As shown in ΔF/F0 graph, the fluorescence level spikes starting from neurite bundle (1) to post-synaptic neurons (2 to 5). The scale bar indicates 200 μm (B), 50 μm (C. i, iii, iv), 1 μm (C. ii) and 100 μm (D).

Figure 4-1. Microfluidic platform for neurovascular unit (NVU) including blood-brain barrier (BBB). (A) The neurovascular unit includes a highly selectively permeable vascular feature called the blood-brain barrier which is composed of a complex network of capillaries and astrocytes. The astrocytes are directly interfaced with the capillaries through astrocytic endfeet, which anchor the neurons to the vascular network. Adjacent to the BBB are neural circuits composed of synaptic neural networks. (1) Proposed in vitro 3D NVU platform. The in vitro NVU platform consists of an engineered BBB co-culture of astrocytes integrated into a vascular network, and a neuronal network “interior” to the BBB. The vascular network component is generated first in the dedicated Vascular Network Channel (VNC). As the vascular network forms, individual lumens form in the area between each posts on the Vascular Channel (VC) for VNC bound media. Neural cells are applied to the Neural Channel side of the nascent vascular network. (“Neural channel”, NC) of the VNC (2, 3). (B) The process of platform generation. The perfusable vascular network is formed over a 3-day period via vasculogenesis protocol. The lumen of the vascular network is not yet open to the VC at this time (1). A suspension of freshly isolated neurons and astrocytes is

loaded into the NC side of the VNC by applying the cell suspension to the NC media channel and tilting the device in such a way that flows the neurons and astrocytes towards the VNC posts and causes them to settle on the VNC/NC border posts (2). The VC and NC media channels are supplied with their respective optimized media, allowing for the formation of the BBB tissue within 5 to 7 days (3).

Figure 4-2. Comparison of three neuron cultures in NBMB27, NBMFBS, and EGM for assessing the effect of FBS in neural cultures. (A) Immunostained images of each experimental medium culture. (B) The total number of nuclei and synapses identified in each culture. As the neurons were grown in a mass against the fibrin hydrogel wall and do not migrate, synaptic connections were measured at the cell mass. (C) The per neuron average of synaptic connections value for NBMFBS was found to be similar to that of cultures grown in NBMB27 control. EGM supplied neuronal cultures show a drastic decrease in synaptic connectivity.

Figure 4-3. The effect of VEGF-A on the proliferation of astrocytes. Unlike EGM, NBMB27 and NBMFBS do not have VEGF. Astrocytes also proliferate prominently in EGM condition but less proliferate in NBMB27 condition and NBMFBS condition. On the other hand, the proliferation of astrocytes is observed when VEGF-A (100 ng/ml) is added to NBMB27 or NBMFBS.

Figure 4-4. Comparison of vascular network and astrocyte areas in experimental medium co-culture conditions. (A) CD31 stained vascular networks shown in red, GFAP stained astrocytes shown in white for all three experimental medium compositions (annotated in VC/NC supplied channels): EGM/NBMFBS; EGM/EGM; 5:5 mix of NBMFBS:EGM for both channels. Vascular network bound media was supplied through the Vascular Channel

(VC), and neuron bound media was supplied through the Neural Channel (NC). In the presence of EGM, astrocytes exhibited increased proliferation and migratory behavior. Astrocytes were observed to migrate from the initial neural cell suspension injection zone to the border of the vascular network. (B) Average area occupied by the vascular network between a pair of parallel microposts. In cultures where VC was supplied with ECM, (EGM/NBMFBS and EGM/EGM), vascular network areas were roughly equivalent. (C) Average area occupied by astrocytes between a pair of parallel microposts. Cultures supplied with NBMFBS via the NC, exhibited the highest astrocytic areas.

Figure 4-5. Linear gradient inside fibrin hydrogel before lumen of vascular network opens to medium channel. (A) The vascular network was cultured in the fibrin hydrogel for 3 days. The lumen of the vascular network is still not connected to the medium channel. Therefore, the wall surface of the fibrin hydrogel is still maintained. At this point, neural cells are attached to one side of the fibrin hydrogel. FITC-dextran was injected into the medium channel opposite to the neural cell. (B) At this time, FITC-dextran (20 kDa) gradient across the fibrin hydrogel is not affected by the vascular network. FITC-dextran shows a linear gradient in the fibrin hydrogel. (C) Diffusion profile inside of fibrin hydrogel. This diffusion profile was measured 10 minutes after FITC-dextran injection.

Figure 4-6. Area difference of vascular network and astrocytes under various conditions. In this experiment, the medium in VC and NC is the same. Reduced amount of EGM in the medium micro-channels makes smaller area of the vascular network. However, reduced amount of EGM in the medium micro-channels makes the larger area of the astrocytes.

Figure 4-7. Immunostained imaging of the vascular network -

astrocyte interface. (A) Astrocytic migration from the NC side neuron-astrocyte loading suspension follows the VEGF gradient towards the VC, and stops after directly interfacing with the vascular network. The neuronal synaptic network is clustered to the right of the fibrin gel, adjacent to the astrocyte-vascular interface. (B) An intermediate section layer of the NVU platform. Vascular network lumens form between each VC facing micropost, with each opening occupying the space of the entire post gap. The vascular network is perfusable from the VC, but is not connected to the NC. (C) Imaging of the direct vascular network-astrocyte interface. Confocal microscopy confirmed direct contact on two axes, with contact points indicated in the xz plane render via arrow points. (D) Vascular network - astrocyte contact confirmed through immunostaining for ZO-1 tight junction protein expression by CD31 positive endothelial cells.

Figure 4-8. Direct contact of the vascular network and astrocytes. A large number of direct contacts between vascular network and astrocytes is observed not only xz plane but also yz plane (arrowhead).

Figure 4-9. Direct contact between vascular network and astrocytes under various conditions. In this experiment, the medium in VC and NC is the same. Although medium conditions are different, a number of direct contacts occurs.

Figure 4-10. Expression of aquaporin 4 at the direct contact between vascular network and astrocytes. (A) Immunostained image of vascular network (B) Immunostained image of astrocytes (C) Immunostained image of aquaporin 4. The red dotted line represents the outline of the vascular network. The aquaporin 4 is mostly expressed on the vascular network. (D) Merged image of vascular network, astrocytes, and aquaporin 4. (E) The aquaporin 4 is expressed at the direct contact between vascular network and astrocytes.

Chapter 1. Introduction

Central nervous system of vertebrates consists of the brain and spinal cord [1]. Among them, the brain that performs a comprehensive function controls the complex behavior of vertebrates. The brain tissue is so complex that it is still not fully known. The human brain consists of about 100 billion neurons and 10 times more glial cells such as astrocytes, oligodendrocytes, and microglia [2]. In addition to this, endothelial cells that make up the blood vessels and ependymal cells that make up the ventricles also exist in the brain tissue [3, 4]. The various and numerous cells present in the brain are not randomly arranged but form delicate and complex structures. Two representative structures of the complex brain are the neural circuits and the blood-brain barrier [5, 6]

The neural circuit consists of neurons. Each neuron forms synapses with hundreds of other neurons to form a neural network that exchanges complex information [7]. Neuronal connections in the neural network are not random. Neuron groups that constitute each region of the brain accurately project

axons into the destination neuron group. There are two kinds of methods in which the orientation of the neural networks can be established during the development of the brain. One is chemical signaling, typically netrin attracting axons and slit repulsive axons [8, 9]. In addition to the chemo-gradient method, there is another method in which the orientation of the axons is determined by the stiffness of the tissue substrate. This method is based on the mechanosensing of axons which grow from a stiff substrate to a soft substrate [10]. The axons of the neural network have structural features that exist in a fasciculated form rather than being individually located until they reach their destination. When the Axon bundle arrives at its destination, it is defasciculated and forms a synapse at the appropriate neurons [11]. Based on these structural features, neural signals can be successfully transmitted in one direction in the neural network.

Unlike the capillaries in the body, the capillaries present in the brain are contacted by astrocyte. Structural features that cannot be seen in the blood vessels of these other tissues lead to a functional characteristic that the permeability of capillaries is extremely low [12]. Due to this low permeability, substances in the blood cannot be transferred to the brain tissue, which is

called the blood-brain barrier. Blood-brain barrier can protect brain tissue from toxic substances, but conversely, it is also restricted by blood-brain barrier to deliver drugs to brain tissue.

Application of microfluidic technology to neuroscience application enables control and manipulation of micro-environments around neurons in both spatial and temporal manner. An organ-on-a-chip using the microfluidic platform is capable of achieving what cannot be achieved in a conventional cell culture environment. Conventional cell culture has been performed in a two-dimensional environment such as a petri dish or a coverslip. This environment differs from the *in vivo* environment. In order to overcome the two-dimensional environment, 3D cell culture method using ECM hydrogel or cell spheroid has been developed similar to the *in vivo* environment, but it is also difficult to control and observe the tissue [13]. Brain tissue will also overcome all of these shortcomings if it is developed on a microfluidic platform.

Recently 3D neuronal culture systems in microfluidic attract attention as a more physiologically relevant model for investigating cellular and

molecular behaviors, channel functions, and neurological disorders (Fig. 1-1). Engineering hydrogels as 3D substrates is being evolving to a new *in vitro* model to mimic brain structure for understanding neural disease and neural function. 3D tissue modeling of the brain was planned by introducing two brain tissue features, a neural network and a blood-brain barrier, into the 3D microfluidic platform, respectively. Both models aimed to mimic both the structural and functional features of the *in vivo* brain. In order to simulate the neural network, we try to induce changes in the internal density of the ECM substrate in which the neurons are cultured. The axons are assembled on a soft substrate and fasciculated to simulate the axon bundle structure. Finally, we try to confirm synapses with other neuronal groups. In order to mimic blood-brain barrier, another feature of the brain, we would like to create an environment that provide a suitable culture medium for vascular network and astrocyte respectively. And we try to confirm that the blood-brain barrier formed on the platform has a similar level of permeability to *in vivo* blood-brain barrier.

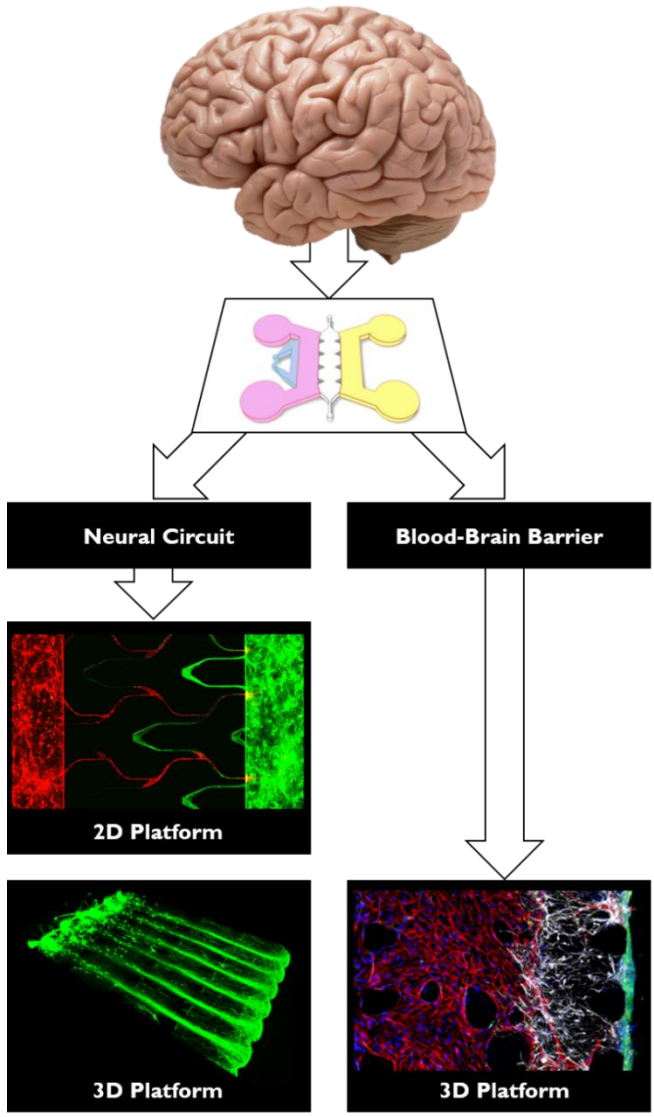

Figure 1-1. Brain-on-a-chip using microfluidics. The two distinctive structures of the brain are the neural circuit and the blood-brain barrier. Each can be mimicked structurally and functionally on a microfluidic platform.

In *Chapter 2*, we describe a microfluidic culture platform that directs the growth of axons using "neural diode" structures to control neural connectivity. This platform is compatible with live cell imaging and can be used to (i) form pre-synaptic and postsynaptic neurons by directional axon growth and (ii) localize physical and chemical treatment to pre- or postsynaptic neuron groups (i.e. virus infection and etc.). The "neural diode" design consist of a microchannel that split into two branches: one is directed straight toward while the other returns back toward the starting point in a closed loop to send the axons back to the origin. We optimized the "neural diode" pattern dimension and design to achieve close to 70% directionality with a single unit of the "diode". When repeated 3 times, near perfect (98–100% at wide range of cell concentrations) directionality can be achieved. The living neural circuit was characterized using Ca imaging and confirmed their function. The platform also serves as a straightforward, reproducible method to recapitulate a variety of neural circuit *in vitro* that were previously observable only in brain slice or *in vivo* models. The microfluidic neural diode may lead to better models for understanding the neural circuit and neurodegenerative diseases.

In *Chapter 3*, we report a microfluidic model of a simplified 3D neural

circuit. First, the microfluidic device is filled with Matrigel and continuous flow is delivered across the device during gelation. The fluidic flow aligns the extracellular matrix (ECM) components along the flow direction. Following the alignment of ECM fibers, neurites of primary rat cortical neurons are grown into the Matrigel at the average speed of 250 μm d^{-1} and form axon bundles approximately 1500 μm in length at 6 days *in vitro* (DIV). Additionally, neural networks are developed from presynaptic to postsynaptic neurons at 14 DIV. The establishment of aligned 3D neural circuits is confirmed with the immunostaining of PSD-95 and synaptophysin and the observation of calcium signal transmission.

In *Chapter 4*, we report a novel three dimensional blood brain barrier (BBB) platform developed by independently supplying different types of media to separate cell types within a single device. One channel (vascular channel, VC) is connected to the inner lumen of the vascular network while the other supplies media to the neural cells (neural channel, NC). Compared to co-cultures supplied with only one type of medium (or 1:1 mixture), best barrier properties and viability were obtained with culturing HUVECs with endothelial growth medium (EGM) and neural cells with neurobasal medium

supplemented with fetal bovine serum (NBMFBS) independently. The measured vascular network permeability were comparable to reported *in vivo* values (20 kDa FITC-dextran, $0.45 \pm 0.11 \times 10^{-6}$ cm/s; 70 kDa FITC-dextran, $0.36 \pm 0.05 \times 10^{-6}$ cm/s) and a higher degree of neurovascular interfacing (astrocytic contact with the vascular network, GFAP-CD31 stain overlap) and presence of synapses (stained with synaptophysin). The BBB platform can dependably imitate the perivascular network morphology and synaptic structures characteristic of the NVU. This microfluidic BBB model can find applications in screening pharmaceuticals that target the brain for in neurodegenerative diseases.

Chapter 2. Microfluidic Neural Axon Diode

Published in Technology, 2016, 4, 240 (14)

2-1. Introduction

As one of the most complex structures in the human organism, the brain consists of numerous types of neurons that are interconnected in specific orders [15, 16]. These interconnections form the electrophysiological circuit transferring neuronal signals to target areas [17]. Essentially, each “circuit” has a direction for the flow of a signal. In this respect, an *in vivo* neural network also has highly ordered neural interconnections [18, 19]. Various experimental models satisfying these characteristics have been proposed by many researchers [20, 21]. These models range from the individual whole-animal scale, allowing natural anatomical structure but lacking fine observation and restricted application at the dissociated cell level, to the cellular scale, combining various features but lacking the ordered

connectivity on a larger scale [22, 23, 24, 25].

In particular, diverse *in vitro* experimental models provide different environments, including physical, chemical, and cell-to-cell interactions, compared with *in vivo* conditions [26, 27, 28]. These distinctions between the *in vitro* and *in vivo* situations induce different connections in reconstructing neural networks in dissociated cell cultures [29, 30, 31]. The neurons typically cultured in plastic cell culture plates reconstruct a neural network randomly and suffer from experimental limitations [32]. Because the neurons are highly polarized and construct ordered networks, conventional cell culture models in petri dish present challenges in studying neuron signal transfer [33].

Several approaches have been suggested to reconstruct neural networks from dissociated cells cultured *in vitro* [34, 35]. However, these models are limited in forming essentially a random network that differs from that of the original polarized network. To overcome these limitations, research groups have proposed several methods to form a directional neuron circuit. Peyrin *et al.* suggested a microfluidic device consisting of two individual cell culture chambers and asymmetric funnel-shaped microchannels [36]. This microchannel design allows the polarized axon structure through axonal

engorgement in a narrowing section. Thibault *et al.* reported a method to inhibit or permit axon passage by switching a pair of electrode gates on or off [37]. Feinerman *et al.* reported the asymmetric geometry patterning which allows only forward propagation of neural signal [38]. However, these methods have several limitations, such as complex fabrication process or allowing partial backward axon growth.

Here, we propose a “neural diode” which allows neuron circuit linked to the directional axon growth (Fig. 2-1). The axons have directionality stemming from particular patterns in the microchannel. The key innovation in this device is the design based on the behavior of axon elongation, furthermore it allows for the construction of a neural network in a single direction without any additional cue. We analyzed the behavior of the axons caused by the microstructure, which was the basis of the diode design factors. Moreover, we show that the intracellular calcium signal was propagated from the presynaptic chamber to the postsynaptic chamber, but was not in the reverse direction. Our platform resulted in the achievement of a binary neural network.

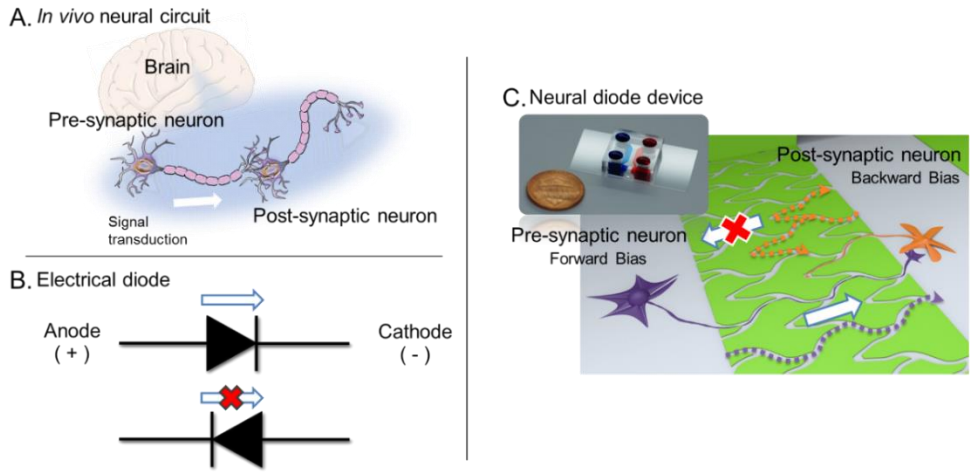

Figure 2-1. Schematic of the conceptual framework for the neural diode. (A) Targeted structure of an in vivo neural circuit. A neural circuit consists of two or more neurons in the brain. To transmit a signal from an activated region to a target systematically, a highly ordered structure is constructed. (B) The function of a diode in an electrical circuit. A diode allows a current to flow through it in only one direction. (C) Microfluidic neural diode platform. It mimics the ordered neural connections in vivo using guiding structures and microchannels. Neurons in the presynaptic chamber can grow into the postsynaptic chamber but the other bias restricts the growth of neurons. The inset shows the neural diode device image.

2-2. Materials and Methods

2-2-1. Fabrication of microfluidic device

We fabricated the microfluidic device in polydimethylsiloxane (PDMS) using soft lithography and replica molding. Briefly, we used photolithography to groove-pattern two layers of SU-8 negative photoresist (Microchem) on a silicon wafer (Unisill Wafer). We pretreated the wafer with air plasma to improve adhesion between the wafer and the photoresist. A master mold was used to manufacture the microfluidic device by casting and curing a prepolymer mixture of PDMS (Sylgard 184, Dow Corning). After curing, the microfluidic device was peeled from the master, and reservoirs were punched out with a biopsy punch (Miltex). We sterilized the device and glass coverslips (24 × 40 mm, Corning Inc.) with ultraviolet (UV) light and 70% ethanol. We activated the surface of the device and a glass coverslip with air plasma (1 minute at 50 W) and brought them together immediately to form an irreversible bond. After assembly, the device channels and grooves were coated with a solution of 1 mg mL^{-1} poly-L-lysine (PLL, Sigma) in

phosphate-buffered saline (PBS, Gibco) for 1 hour. Before use, devices were washed 3 times with sterilized deionized water.

2-2-2. Cell culture

All animal experiments have been conducted in accordance with protocols approved by the Institute of Laboratory Animal Resources (ILAR) at Seoul National University, Korea. We isolated rat cortical neurons from Sprague Dawley embryonic rats (E17-18) according to previously published procedures. The cortex of the embryo was isolated in Hank's Balanced Salt Solution (HBSS, Gibco) and treated with trypsin-EDTA solution (Gibco) for 10 minutes at 37°C. After the supernatant was removed, we rinsed the cortex tissue with HBSS and replaced it with Dulbecco's Modified Eagle's Medium (DMEM, Gibco) containing 10% fetal bovine serum to stop the trypsin reaction. We mechanically separated the cells by trituration through a Pasteur pipette and resuspended the cells in neurobasal medium (Invitrogen) containing 2% B27 supplement (Invitrogen), 0.25% GlutaMax (Invitrogen), and 1% penicillin-streptomycin (Invitrogen). Finally, we collected the

primary neuronal cells by passing the medium through a 40 μm cell strainer. The cells were loaded after the media were removed in the reservoir. A 20 μl of cell suspension was loaded into the channel at density of 6×10^6 cells ml^{-1}. The cells were incubated for 30 minutes, then allowed to settle and adhere on the substrate. After confirming the attachment of cells, we filled the neurobasal medium on the reservoir. The neurons were cultured up to 14 days in fresh media which were changed every two days.

2-2-3. Virus infection

Both recombinant adeno-associated virus vector stocks encoding the GFP or tdTomato protein (Addgene) were generated by transient transfection of 293T cells and purified by CsCl gradients as described previously25. Each recombinant vector was diluted in fully neurobasal medium and put into each microchannel. For preventing diffusion of each vector to the other microchannel, each vector was put into each microchannel at a different time. The height of bare medium in the other side's reservoir was higher than the height of vector side's medium in the reservoir20. After incubating for 10

minutes, the medium with vector was fully washed out. After washing, another vector in diluted medium was then put into another microchannel and washed out as described above.

2-2-4. Fluo-4-AM loading and live cell imaging

For calcium imaging experiments, neurons were dissociated from postnatal day 1 (P1) Sprague Dawley rat hippocampus and plated onto the poly-D-lysine-coated microfluidic device. Neurons were loaded with 1 μM Fluo-4-AM/Tyrode's solution (119 mM NaCl, 2.5 mM KCl, 2 mM CaCl2, 2 mM MgCl2, 25 mM HEPES, and 30 mM glucose, pH 7.4) for 15 minutes at 37°C. Aft er 5 minutes of washing in dye-free Tyrode's, time-lapse images were taken at 2-second intervals for 10 seconds, and high KCl solution (31.5 mM NaCl, 90 mM KCl, 2 mM $CaCl_2$, 2 mM $MgCl_2$, 25 mM HEPES, and 30 mM glucose, pH 7.4) was added to the indicated channel.

2-2-5. Imaging equipment and analysis

Fluorescence images were obtained using an Olympus IX81 inverted microscope (Olympus) equipped with an LED light source (CoolLED) and an electron-multiplying charged-coupled device (EM-CCD) camera (Hamamatsu). Confocal images were obtained on an inverted Zeiss LSM 780 multiphoton laser scanning confocal microscope (Zeiss). Time-lapse images were acquired with an Olympus IX-71 inverted microscope (Olympus, Tokyo, Japan) with a 40×, 1.0 NA oil lens using an Andor iXon 897 EM-CCD camera (512 × 512, 16 bit; Andor Technologies, Belfast, Northern Ireland), driven with MetaMorph Imaging software (Universal Imaging Corporation, West Chester, PA). Light was provided from an LED machine (LCI, Seoul, Korea). Time-lapse images were analyzed using ImageJ and Origin 9.0. During time-lapse imaging, the device was placed on the stage with a live imaging chamber (LCI) to maintain the temperature and humidity. Acquired images were adjusted for brightness and contrast using ImageJ software (NIH).

2-2-6. Statistical analysis

Figures 2 and 3 data were compared using one-way analysis of variance

(ANOVA) followed by Tukey's post-hoc comparisons for repeated measures. A statistical significance threshold was set at 0.05 (with $p < 0.05$). Figure 4 data were examined by paired t-test. All error bars in the figures indicate mean standard error.

2-3. Results

2-3-1. Axon growth characteristics in microchannel

Previous research described a microfluidic device that polarized axons using a microchannel [32]. In that research, when neuron axons came out from the exit of the microchannel, they were determined to extend in a straight direction. We took notice of this phenomenon and studied the axon growth characteristics clearly. We fabricated the microfluidic device for axonal direction analysis (Fig. 2-2). This device had two main channels which were linked with microchannels. The geometry of the microchannels are shown Figure 2-3A. The microchannel was of 3 μm height and 10 μm entrance width. The length and width of the initial part of the microchannel was 400 μm and 10 μm, and it was connected to a broad round-shaped region. To obtain a sufficient growth cone in the filopodia movement area, we expanded the center region in the microchannels. This region of interest (ROI) had a 100 μm radius and multiple exit channels at each 30° angles. We could observe the growth direction-searching process of the filopodium at ROI. Neurons

were plated in main channels and its axons elongated through microchannels. When the axon came out of the initial part of the microchannel, it reached the ROI, allowing the axon to extend anywhere. When the axon entered from the initial part of the microchannel into the ROI, the filopodium seemed to navigate while repeating contraction and expansion over a short time. After the filopodium went through this exploratory state, it became steady state. We observed that axon growth continued in a straight direction in the absence of any particular cue. Figure 2-3B showed the axon distribution at 11 days *in vitro* (DIV). The neurons were fluorescently stained with calcein AM.

Using this fluorescence image, we quantified axon distribution in the ROI (Fig. 2-3C). The covered area of axons in the ROI was recognized by calculating the difference between the calcein AM fluorescent intensity and background signal. This quantification shows the direction of axon growth in the ROI. Most (83.40 ± 13.35%) of the entering axons grew straight, within a range of ±15° from the center line, although the direction of extension was not limited. Upon encountering the opposite wall of the outlet channel, axons grew along the wall and “escaped” the region. The result of single axon growth reported that 16.7 ± 2.5 μmh^{-1} of growth rate, 1.4 ± 2.3° of axon

turning angle and 65% of single axon grew straight within a range of ±5° [40].

Previous research described that axons grew along the microchannel, when the growth cone reached the wall of the microchannel tangentially [34, 36]. Axons encountering the wall of the microchannel could not go through the physical structure such as the PDMS; therefore, they have to grow along the microchannel walls [41].

Our above-mentioned experiment revealed that axons grew in a straight manner in the absence of any external cue. However, after being forced to change the direction of growth by the wall of the microchannel, this property was altered. Therefore, we investigated the threshold distance for maintaining straight directionality after being turned by the wall of the microchannel.

We designed simple fork-shaped microchannels which had 3 μm height and 10 μm width (Fig. 2-2). Each microchannel had straight 700 μm length entrance part, turning points and various lengths (L) of straight channel (Fig. 2-4A). At the turning point, the curved feature forced the axons to turn 30°. The channels led to two fork-shaped channels, either an extended straight channel (channel 1) or an intersection channel (channel 2), which had the same direction as before the turning point. If the axon maintained its straight

direction after passing the turning point, it entered into channel 1, but if not, it entered into channel 2.

In an eff ort to reveal the threshold lengths of straight growth after axon turning points, we established a range from 30 to 240 μm. The axons quantification was performed using the same method as above. As shown in Fig. 2-4B, the directionality of axons (whether they chose channel 1 or 2) highly correlated with the length (L) of the straight channels, whereas short channels, 30–60 μm in length, allowed complete entering into channel 2, extending the length (L), and increasing the number of axons entering into channel 1. The longer the straight channels, the more axons disregarded the branch channels. Thus, the results were 19.85 ± 0.19% of axons for 73.15 ± 1.63% for L = 120 μm, and 86.44 ± 2.66% for L = 240 μm. Figure 2-4C shows a plot of the percentage of axons that retained their directionality after turning as a function of L. Thus, the threshold in length of a straight feature after a turning point (the value of L for which we observed entering through channel 1 at 70%) is ~120 μm.

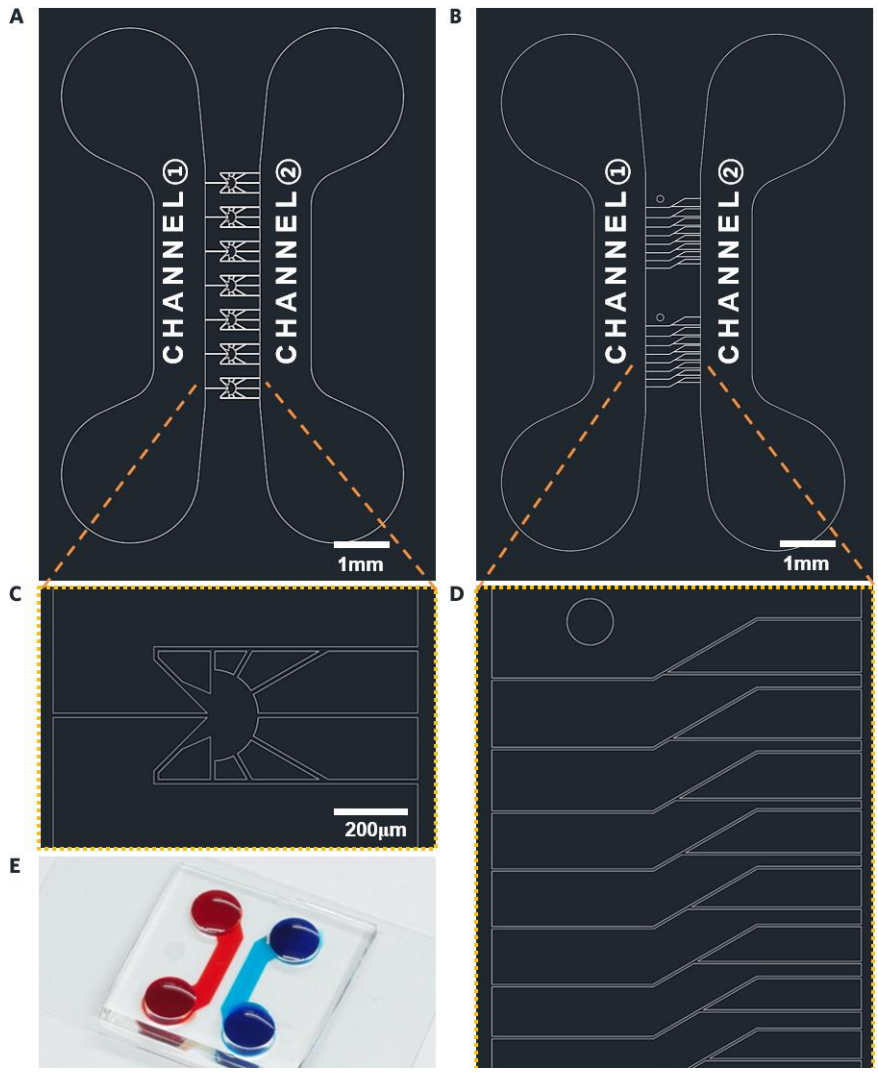

Figure 2-2. Drawing of microfluidic device used in Fig. 2-3 (A and C are the magnified images) and Fig. 2-4 (B and D are the magnified images). The microfluidic devices in this paper have similar structures except for the design of microchannels. (E) Real image of the drawing of the B device.

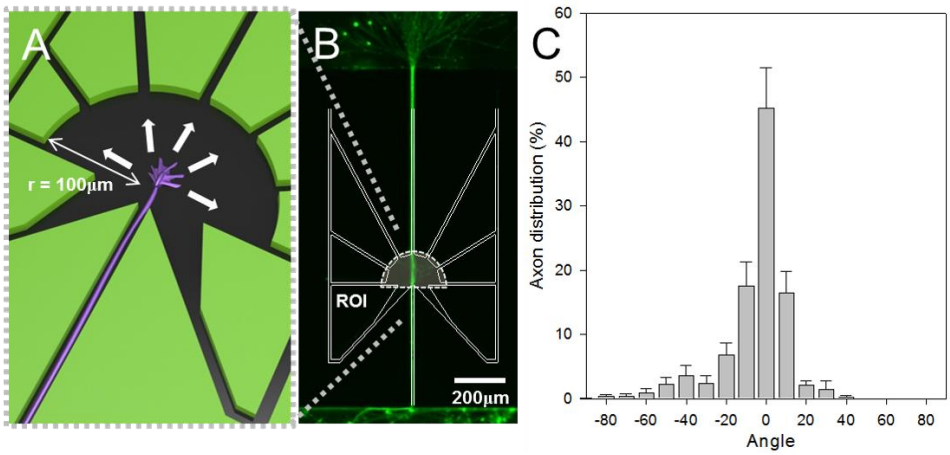

Figure 2-3. Growth cone behavior when encountering open space after growing through a microchannel. (A) Schematic of the microstructure comprising an input channel to an extended region. When the axon terminal comes out of the input channel, it emerges into a large area, allowing growth in any direction. (B) Fluorescence image of a microfluidic culture revealed the directionality of axon growth. We observed axon growth in the region of interest, as marked on the figure. (C) Quantification showed that 83.40 ± 13.35% of axons grew straight (within a range of ± 15° from the center line). Samples are $n > 10$ (number of channels). $F = 35.80$, $p < 0.05$ by one-way ANOVA.

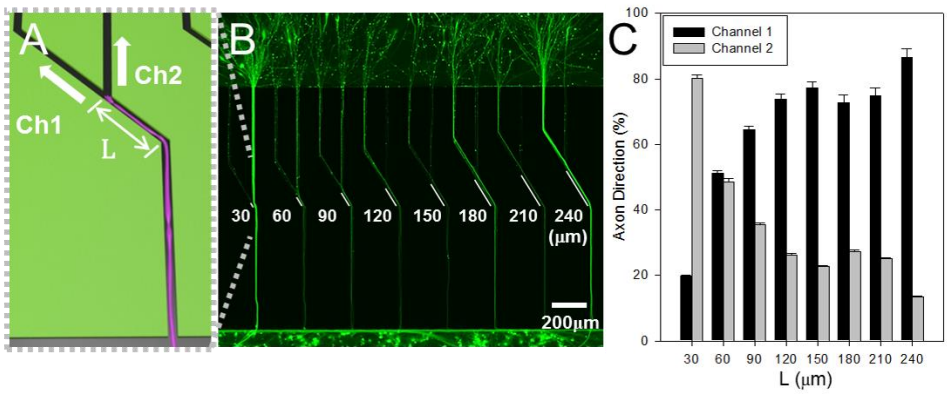

Figure 2-4. Growth cone behavior for maintaining directionality. (A) Schematic of the microstructure comprising two forked channels. When an axon grew out through the microchannel (distance L), it could extend in a new direction (channel 1) or maintain its original direction (channel 2). (B) Fluorescence image of a microfluidic culture to observe maintaining axon growth direction after being turned physically. The microchannel length, from the direction change point to the forked point, was in the range of 30 to 240 μm. (C) Quantification showed that the number of axons growing in the new direction (channel 1) increased significantly as distance L increased. In particular, most axons extended in the new direction (channel 1) when the distance L was more than 120 μm. Samples are $n > 10$ (set number of channels). $F = 14.06$, $p < 0.05$ by one-way ANOVA.

2-3-2. Design of neural diode

The design of the neural diode described in this work was inspired by the Tesla valve or Tesla's valvular conduit. Tesla's valvular conduit is a valve that allows fluid to flow preferentially in one direction [42]. It does not have any moving parts but consists of channels which have asymmetric branches and loops. Due to its asymmetric splitting design, forward fluid can flow with minimum resistance while backward flow is highly disturbed by flow via serpentine branch that combines with the other flow.

From the above experiments, we clarified the variables controlling axon growth: the "straight growth characteristics of axons" and the "required distance" to maintain axon growth direction. On this basis, we proposed the "neural diode".

We tried to exploit these properties to achieve a polarized interconnection in which axons grow from one area (emitting chamber) to another (receiving chamber) and not retrogress. The device was composed of two cell culture chambers, separated by 1000 μm long, 3 μm high microchannels. The microchannels, called the neural diode, were designed as follows. Channel

width was designed from 10 (microchannel) to 50 μm (loop channel) by considering a characteristic of axon growth. Based on the characteristic of extending straight and maintaining the directionality of axons (Fig. 2-3, 2-4), we designed neural diode channels. The result of above experiments shown at Fig. 2-4, the forked shape channel with more than 120 μm distance could control the axon growth to channel 1. Repetition of the forked shape channels forms asymmetrical net-shaped microchannels (Fig. 2-5B box).

In more detail, viewed from the forward bias, axons grew through the microchannel which turned at an acute angle (less than 30 degrees) not at an obtuse angle (Fig. 2-5A). Viewed from the backward bias, axons entered the microchannel and reached the turning point shown as Fig. 2-5B (a). The channel, expressed in Fig. 2-5B a point to b point, was more than 120 μm long to maintain the direction. This length come from the result of the axon growth characteristics experiment as shown in Fig. 2-4. This channel led axons into two channels: one was directed straight toward the opposite receiving channel but the other, leading almost backwards, was destined for a closed loop for backward bias axons (Fig. 2-5B). The channels connected to the closed loop prevented axons from turning back to the emitting channel.

This closed loop channels had the wide width (50 μm) to provide sufficient space for entered axons, since the axon confluent state forced the axon growth into empty microchannels. Viewed from the backward bias, straight growing axons entered the loop channels so that they came back to the receiving chamber. Thus, because the nature of growth was straight, the axons starting from the emitting chamber could enter the microchannel heading for the opposite chamber, whereas axons extending from the receiving chamber entered the loop-shaped microchannel, returning to the chamber (Fig. 2-6).

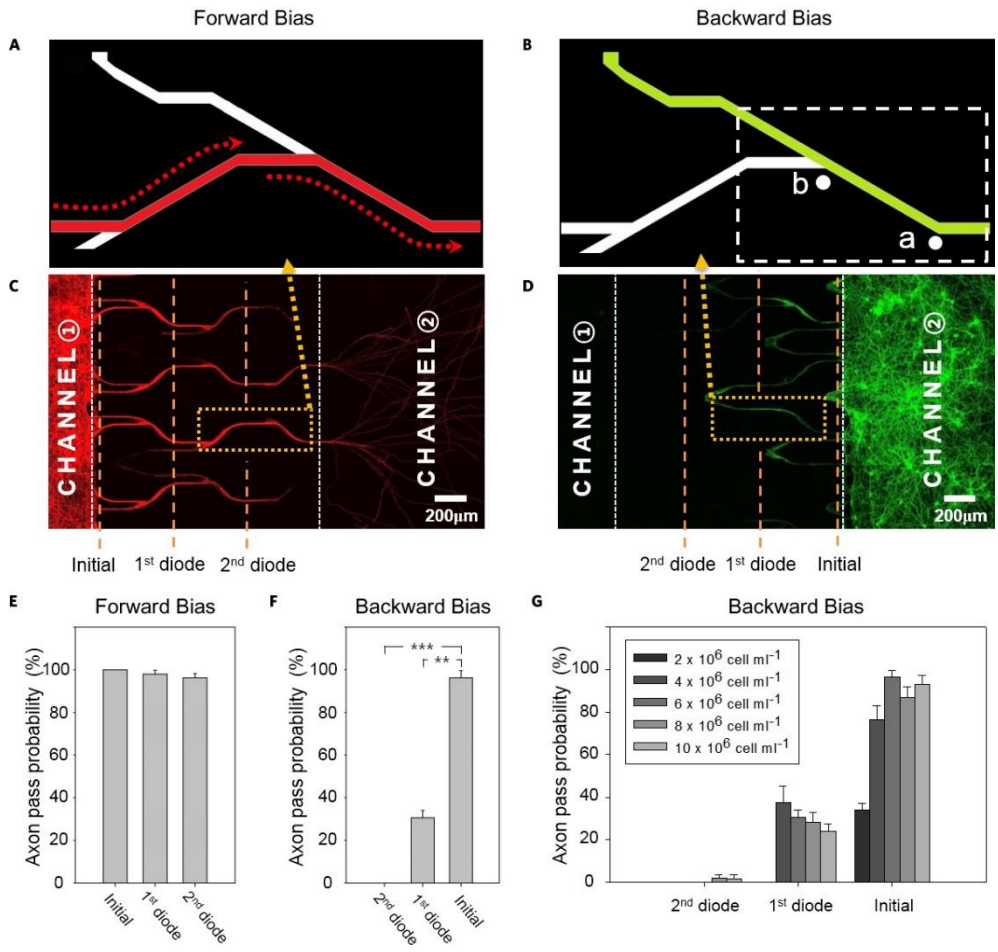
Forward Bias
Backward Bias
A
B
b
a
C
D
CHANNEL①
CHANNEL②
200μm
Initial
1st diode
2nd diode
2nd diode
1st diode
Initial
E
Forward Bias
F
Backward Bias
G
Backward Bias
Axon pass probability (%)
0
20
40
60
80
100
Initial
1st diode
2nd diode
***
**
2 x 10^6 cell ml^-1
4 x 10^6 cell ml^-1
6 x 10^6 cell ml^-1
8 x 10^6 cell ml^-1
10 x 10^6 cell ml^-1

Figure 2-5. In vitro neural network using the "neural diode" in a microfluidic culture device. Design of the forward bias (A) and backward bias (B) neural diode. They are magnified image of C, D. Channel 1 and 2 are seeded with neurons simultaneously and co-stained green/red at 14 DIV. The length of a point to b point is more than 120 μm for retained axon directionality. Fluorescence image of the presynaptic channel 1 and postsynaptic channel 2 in microfluidic cultures. (C) Axons in the presynaptic channel 1 reached the opposite side. (D) However, axons in the postsynaptic channel 2 could not reach the opposite channel 1 due to the effect of the diode repeated three times. (E) Quantification showed that the neural diodes efficiently polarize axonal growth. An axon extending with forward bias could readily pass the diode. (F) However, an axon extending with backward bias could not reach the opposite channel within the second diode. $* < 0.05$, $** < 0.01$, and $*** < 0.001$ paired t-test. (G) When lower cell density is used (less than 6×10^6 cells ml^{-1}), cell viability is adversely affected. For higher cell densities up to 10×10^6 cells ml^{-1} resulted in similar high selectivity of the diode. All samples are $n > 5$ (number of devices).

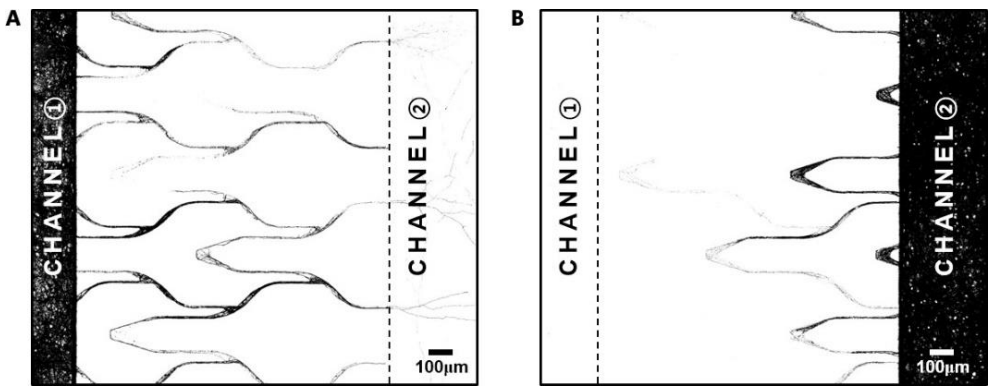

Figure 2-6. To observe clearly whether an axon reached opposite channels, we made a mask of axon distribution based on fluorescence images. (A) Neurons in presynaptic channel 1 could easily extend to postsynaptic channel 2. (B) However, neurons in postsynaptic channel 2 could not reach the presynaptic channel 1 after three times of repeated neuron diode.

2-3-3. Efficiency of the neural diode

To estimate the blocking or passing efficiency of the neural diode, we followed the growth of neurons in the chamber extending into the neural diode microchannel. Moreover, we confirmed the reiteration time of the diode pattern to achieve perfect directionality. We cultured primary rat cortical neuronal cells in each chamber for 14 days. The microfluidic device allowed the isolation of each chamber by volume difference between chambers. Briefly, a volume difference between the emitting and receiving chamber allowed the chemical microenvironments to be isolated from the other chamber for more than 20 hours due to the high fluidic resistance of the microchannel. Fluidic-based isolation of the virus allowed for infecting the axons in the emitting and receiving chambers independently. Figures 2-5C and 2-5D show images of axon growth in each chamber of the microchannel. Forward bias axons in the emitting chamber are stained with TdTomato (red) and backward bias axons in the receiving chamber are stained with aavGFP (green). Axons in the forward bias microchannel reached the other side by passing through two diode structures.

Using the neural diode, 14 days after cell seeding in the emitting chamber, the axons surged into the receiving chamber, which acted as a postsynaptic neuron group. In contrast, when neurons were plated in the receiving chamber, the axons reaching the opposite chamber were almost perfectly blocked. From this test, we observed that the axon could easily reach the receiving chamber passing through the diode microchannel with a forward bias, whereas an axon growing with a backward bias could not reach the opposite channels within the second diode. We quantified the axon passing probability through the first diode and the second diode at 98.0 ± 1.8% and 96.2 ± 2.1%, respectively (Fig. 2-5E). However, the probability of passing backwards through the first and second diodes appeared to be 30.6 ± 3.5% and zero (closed), respectively (n > 30; Fig. 2-5F). The neural diode was tested in triplicate.

We also quantified neural diode efficiency for different neuron seeding densities (Fig. 2-5G). Briefly, low cell concentration state had negative effect on viability of cells and decreased growth of axons. It led to a low number of axons entering the microchannels. With concentrations higher than that of 8 × 106 cells ml−1, the probability of passing backwards through the first and second diodes appeared to be 28.3 ± 4.5% and 2.0 ± 1.8%. (Specifically, 24.2

± 3.2% and 1.8 ± 1.7% for cell concentration of 1×10^7 cells ml^{-1}.)

Additionally, the axons grew to the forward microchannel which turned 30 degrees or less in the early state of growth. But, axons became confluent in microchannel as the number of axons entering the microchannel increased. This confluent state forced the axon growth to empty from the microchannel which then extended to backward by almost 150 degrees. This axon turning back seemed different from the result. But the above-mentioned axon growth characteristics were based on observation without any physical force. Thus, when a large number of axons complicate the microchannels, they grew to the quieter microchannels, even those that were extremely turned back. Due to these axon growth characteristics, we designed sufficient loop space in the microchannel for prevention against growth. The return microchannel formed the loop with another return microchannel. It can be found between the 1st diode line and the 2nd diode line in Figs. 2-5C and 2-5D.

2-3-4. Intracellular calcium imaging

To monitor functional synapse formation directly in the microfluidic device, we loaded the neurons with Fluo-4-AM Ca2+ dye and treated them with high KCl to stimulate neurons located on the other side of the microfluidic chamber (Fig. 2-7B). The microfluidic device enabled the microfluidic isolation of axonal microenvironments by achieving volume differences between the two chambers due to the high fluidic resistance of the microchannels [34]. The resistance established a minute sustained flow, which neutralized diffusion [35]. After stimulating the neurons, the neurons on the other side showed Fluo-4-AM signal increases simultaneously (Fig. 2-7C–E). This indicated that the axons passed through the microchannel and made functional synapses with neurons on the other side. To assess whether the microfluidic neural diode truly induced one-directional axon growth, we performed the same experiment with the inverse treatment of high KCl and Fluo-4-AM (Fig. 2-7F). As a result, we confirmed that, in the reverse direction, there was no functional synapse because axons in the reverse direction could not reach the other side of the channel (Fig. 2-7G–I). Collectively, these

results indicated that neurons in the microfluidic device had one-directional axon growth and these directional axons formed functional synapses with dendrites of the neurons on the other side.

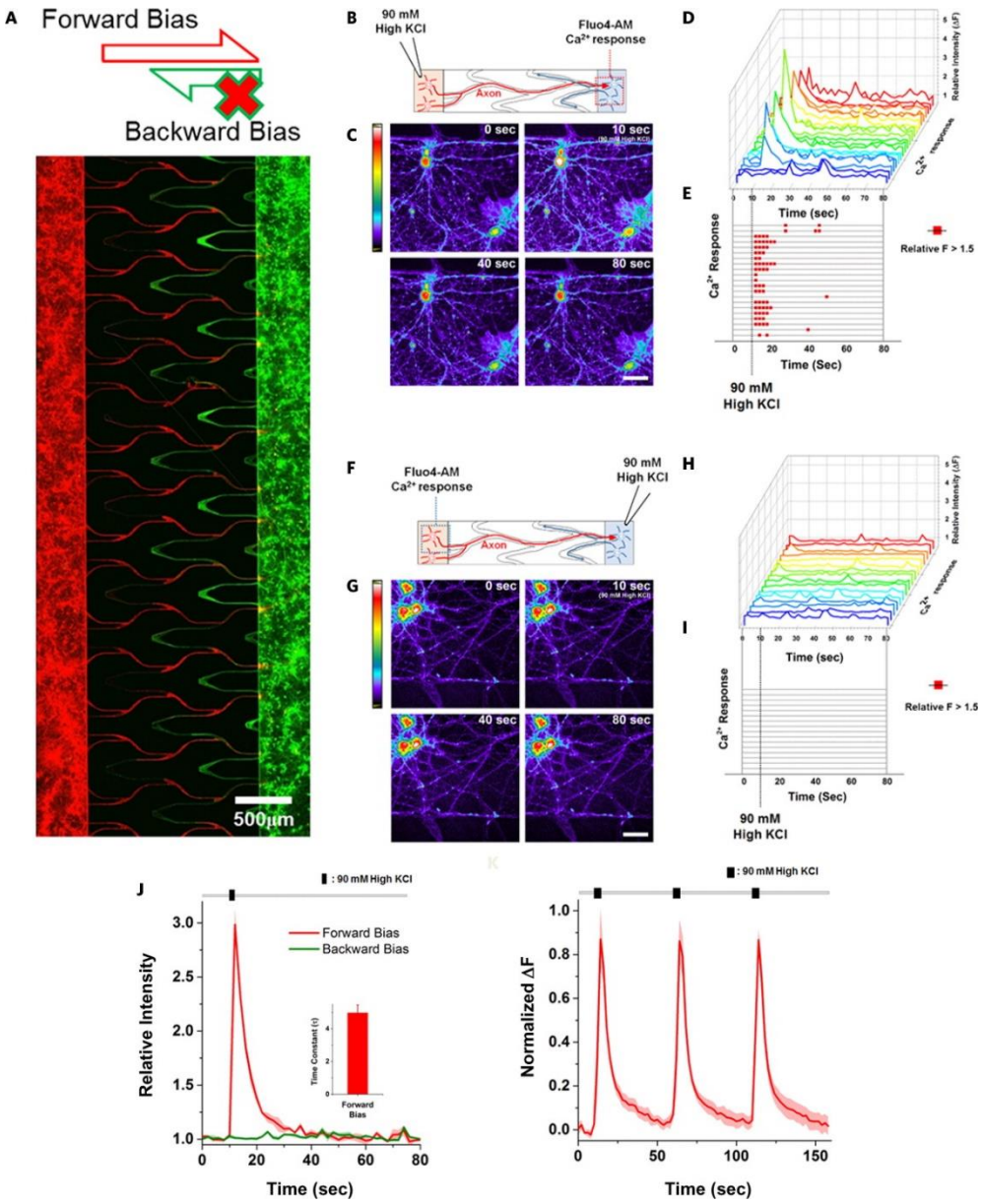
A
Forward Bias
Backward Bias
500μm
B
90 mM
High KCl
Fluo4-AM
Ca2+ response
Axon
C
0 sec
10 sec
40 sec
80 sec
D
Relative Intensity (ΔF)
Ca2+ response
E
Time (sec)
Ca2+ Response
Relative F > 1.5
Time (Sec)
90 mM
High KCl
F
Fluo4-AM
Ca2+ response
90 mM
High KCl
Axon
G
0 sec
10 sec
40 sec
80 sec
H
Relative Intensity (ΔF)
Ca2+ response
I
Time (sec)
Ca2+ Response
Relative F > 1.5
Time (Sec)
90 mM
High KCl
J
: 90 mM High KCl
Forward Bias
Backward Bias
Relative Intensity
Time Constant (τ)
Forward Bias
Time (sec)
: 90 mM High KCl
Normalized ΔF
Time (sec)

Fig 2-7. (A) Image of the whole neural diode device (red: forward bias, green: backward bias). (B) Schematic images for the experimental protocol (microfluidic neural diode: normal direction) used in C–E. (C) Representative time-lapse images for the Fluo-4-AM Ca^{2+} response before and after a brief (2-second) treatment with 90 mM high KCl on the other side of the microfluidic channels. (D, E) Representative 3D plot for the Ca^{2+} response. Red boxes indicate the time points above arbitrary threshold (fluorescence increased more than 50% versus the initial fluorescence). (F) Schematic images for the inverse experimental protocol (microfluidic neural diode: reverse direction) used in G–I. (G) Representative time-lapse images for the Fluo-4-AM Ca^{2+} response before and after treatment with 90 mM high KCl on the other side of the microfluidics. (H–I) Representative 3D plot for the Ca^{2+} response. Note that there are no activated neurons by 90 mM high KCl, treated on the other side of the microfluidics. Small and unsynchronized Ca^{2+} peak showed spontaneous activity of neurons. (J) Statistical analysis for B–I. In the forward bias stimulation, we measured decay time constant (τ) for Ca^{2+} clearance (4.67 ± 0.48 seconds). (K) Successive Ca^{2+} responses during multiple treatments with 90 mM high KCl. Presynaptic neurons were

stimulated with a three consecutive 5-second treatment with high KCl, each followed by 45 seconds of resting period.

2-4. Discussion

There are several *in vitro* neural network models that isolate the soma of neurons from axons. They allow reconstruction of a duplex network between two chambers or a hippocampal autosynapse [44, 45]. In the brain, however, neurons are part of complex networks with highly ordered neural interconnections and topologies. Forming directional network with various types of neurons will be the key challenge for mimicking any *in vivo* architecture using microfluidic or other *in vitro* methods. There are few models that can be used to form *in vitro* directional networks but they have limitations that have not yet been resolved. These models used various methods such as positive or negative chemotaxis, magnetic fields, patterning, and microstructures to control the direction of axon elongation [36, 37, 46, 47]. Some of these methods could affect the biochemical expression or metabolism of neurons. In this study, we propose a neural diode device, allowing reconstruction of a simplex neural network connection using physical features. This platform has various advantages over existing methods, including no need for chemical cues and the ability to obtain the same results

from diverse cell concentrations and pharmacological treatments. Using this platform, we can achieve directional network with good reproducibility regardless of other variables, such as cell number density. Our results show axonal morphologies and morphodynamics in response to modified microfluidic devices, indicating that oriented axons maintain their directionality.

Growth of the growth cone can be divided into a latency period and an interaction period, as proposed in the “molecular clutch model” [48]. In the latency period, filopodia, organelles to sense and adhere to a substrate or structures, engage in an active search process for a molecular “clutch” between attractive molecules in the surrounding environment and receptors. Filopodia stochastically scan the surroundings with repeated protrusion and retraction. Moreover, some F-actomyosin networks built in the peripheral domain are associated with microtubules and the others are involved in actin recycling. The linkage tension of the F-actin network in the peripheral domain and microtubules in the central domain is not strong and sustains retrograde F-actin flow. As a result, growth is slow. In the interaction period, receptors that are functional clutch with molecules, allowing increased central-

peripheral domain tension. This leads to attenuated retrograde flow and robust invasion of central domain microtubules. Newly localized microtubules in central domains are compressed by myosin II contained in actin arcs [49].

From the results described herein, we assume that once an axon enters the interaction period from a latency period, it maintains the molecular clutched state and protrusive growth until detecting sudden changes in the ambient environment. Specifically, the axon continues to grow, in the same direction, so long as it is not affected by factors such as physical structures and chemical cues.

The device described herein requires relatively simple microfabrication technology compared with other methods. Diodes using a magnetic field need a thin electrode on a substrate, and other methods using asymmetrical funnel-shaped microchannels involve complex microfabrication steps [36]. The neural diode we are proposing, however, is relatively easy to fabricate, requiring only several tens of micrometers scale-size features and resolution using 2-layer photolithography step. Using soft lithography, hundreds of replicas can be produced once the master molds are prepared. Also, many existing protocols for experiments in the microfluidic system are possible.

2-5. Summary

In this study, we designed and demonstrated an *in vitro* microfluidic neural diode, allowing a simple network connection between pre- and postsynaptic neurons. This directional neuron network not only mimics *in vivo* architectures, but also activates synaptic connections physiologically. This device has several desirable characteristics, as follows. First, it does not require chemical cues to control the growth direction of the axons. Second, axon directionality can be achieved almost perfectly through the simple physical structure. Third, pre- and postsynaptic chambers have separate (independent) microenvironments due to the microfluidic-based isolation. Finally, it is easy to observe the whole process during the development of axons and the synapse.

In vitro reconstruction of polarized neuronal networks is expected to be useful in various applications. Because almost all *in vivo* neural architectures involve biased networks, the microfluidic neural diode platform will be a valuable tool to investigate the molecular and cellular mechanisms in synaptic regions and neural dysfunction, such as in Alzheimer's and Parkinson's

diseases. Especially, the combination of a polarized neural circuit using a microfluidic platform with multi-electrode systems or optical experimental setup (i.e. optogenetics) can enable extension into electrophysiological and pharmacological research. The development of a microfluidic neural diode platform that can recapitulate a variety of neural circuits *in vitro* that were previously observable only in brain slice or *in vivo* models will be useful in a number of neuroscience research topics.

Chapter 3. Engineering-Aligned 3D Neural Circuit in Microfluidic Device

---

Published in Advanced Healthcare Materials, 2016, 5, 159 (30)

3-1. Introduction

In vitro models that allow cells to grow in highly controlled microenvironments have been increasingly used in investigating cell behaviors [50, 51, 52, 53]. 3D *in vitro* culture models of neurons have been reported with various materials such as beads, silk, biocompatible hydrogels, and silicon as the scaffold or matrix, respectively [54, 55, 56, 57]. Significant advances in engineering hydrogels as scaffold material resulted in 3D cell-based models for a variety of tissues [58, 59, 60, 61]. The 3D *in vitro* models were able to maintain several advantages of *in vitro* culture, as well as recapitulate many critical aspects of native tissue, since the hydrogels offered high water content, biocompatibility, and chemical/physical properties [62, 63, 64]. Specifically, methods developed within the two past decades could

lead to 3D *in vitro* models of brain tissue, due to showing longer neurite outgrowth, higher density network, and greater survival rate than 2D monolayers [65, 66, 67, 68, 69]. Most of these studies have been performed with either encapsulating neurons directly into hydrogels or seeding them onto the gels [70, 71, 72].

The existing methodology has limitations in mimicking the intact brain tissue whose structural features are not only composed of the layered structure, but also the neural bundle formation including in fasciculation and defasciculation [11, 73, 74]. A few 3D hydrogel reconstruction techniques were suggested to produce only the layered structure of brain tissue on chip. Collagen type I fiber orientation technique using collagen gel's flow and microchamber for alternating layers with soma and neurite outgrowth was reported [75]. Engineering silk scaffold also allowed 3D compartmentalized neuronal culture [55]. However, mimicking other properties such as neural bundle, usually observed in the *in vivo* brain tissue, into the *in vitro* chip still remain a challenge. We previously reported a gelation method for patterning throughout the depth of the Matrigel hydrogel using the media's flow in a microfluidic device. Implementation of neural circuits in a 3D culture with axonal properties of *in vivo* models has not yet been demonstrated.

Here, we therefore developed mimicking the 3D architecture of the *in vivo*

neural bundle and axon fasciculation, as well as neural circuits with the hydrostatic pressure to change the cross-linking density patterns of hydrogels. We introduced a new pillar type and an array design for multilayered neuronal structure in the microfluidic device and an innovative method to apply stably the hydrostatic pressure into the Matrigel for a long time. The extracellular matrix (ECM) components in Matrigel showed sagging in the pressure direction, and the Matrigel cross-linking density distribution inside the gels was patterned such that the compact density and the sparse density alternated. Neurites grew towards the sparse hydrogel cross-linked area and converged into the sparse area inside the Matrigel. The geometry and the channel number in the microfluidic device dictated these properties. When plating neurons on the one sidewall of the deformed Matrigel, we found that the axon bundle was formed with fasciculation at long distance for 6 d. Additionally, axons were defasciculated at the terminal of the axon bundle. Furthermore, 3D neural circuits were confirmed with the immunofluorescence staining and the Ca^{2+} signal transmission, when neurons were cultured on both side channels in the microfluidic device.

3-2. Materials and Methods

3-2-1. Microfluidic device fabrication

The master mold wafer was fabricated in photolithography with SU-8 negative photoresist (MicroChem, USA) and silicon wafer (Unisill Wafer, Korea). A master mold is used to manufacture the microfl uidic device by casting polydimethylsiloxane (PDMS) (Sylgard 184, Dow Corning, Korea). We poured PDMS on the master mold to 1.5 mm. After fully curing for 30 min in 95 °C, the plastic reservoirs were glued on PDMS and the PDMS was poured to a thickness of 6 mm. The fully cured PDMS microfluidic device was then peeled from the master mold. Sterilized glass coverslips and PDMS microfluidic devices were treated with air plasma to bond permanently to each other. After bonding, we put the microfluidic devices in an 80 °C oven for one week to make the channel surfaces hydrophobic. After one week, microfluidic devices are cooled at room temperature. We placed Matrigel in liquid state to the first ECM hydrogel channel in room temperature for 10 min. We repeated the steps for the second and third ECM hydrogel channels. To make both medium channel surfaces hydrophilic, we filled the medium into the reservoirs and pulled from the opposite reservoir by suction. We filled

more medium to the plastic reservoirs until the water level was at 12 mm and removed the medium completely from the opposite medium channel without the plastic reservoirs. We kept the microfluidic devices in a 37 °C incubator for 3 h until Matrigel was pushed out to the medium channel. The water level stayed the same in both medium channels and the microfluidic device was kept in a 37 °C incubator until neuronal cell plating.

3-2-2. Primary neuron culture preparation

Rat cortical neurons were prepared from a Sprague–Dawley embryonic rat (E17). The rat embryo cortexes were incubated for 10 min at 37 °C in a trypsin-EDTA solution (Gibco, USA). After incubation, the supernatants were removed and Dulbecco's modified Eagle's medium (Gibco, USA) containing 10% Fetal Bovine Serum was added to stop the trypsin reaction. The supernatants were removed again before Neurobasal medium (Invitrogen) containing 2% B27 supplement (Invitrogen, USA), 0.25% GlutaMax (Invitrogen), and 1% penicillin–streptomycin (Invitrogen, USA) were added. The cortexes were triturated with a glass pipet. Finally, cell suspension was filtered with a cell strainer and the required concentration was made by adding neurobasal medium. Cell suspension was placed in a 50 μL microfluidic

device. The microfluidic devices were kept in a 37 °C incubator that tilts 90° to settle the cells down to the Matrigel surface. All experiments were conducted according to the guidelines of the Institutional Animal Care and Use Committee of Seoul National University.

3-2-3. Visualization

SEM imaging of the micropillar array were obtained using the Hitachi S-4800 (Hitachi, Japan) with 10 kV beam intensity and 12 mm working distance. In order to avoid the electron charging effect, all polymer samples were sputter-coated with Pt to a thickness of 10 nm prior to measurements. Confocal images were observed with a FluoView FV1000 confocal laser scanning unit and confocal PMT detector. BAPTA AM stained cells were observed with an inverted microscope (IX81, Olympus, Japan) equipped with an LED light source (CoolLED, USA). Images were taken with ORCA-ER charge-coupled device camera (Hamamatsu, Japan) and an appropriate excitation and emission filter set that uses MetaMorph imaging software (Universal Imaging, Japan). The images were adjusted for brightness and contrast using the ImageJ.

3-2-4. Intracellular calcium live imaging

Intracellular Ca^{2+} live imaging was done with Oregon Green BAPTA-1, AM (OGB, Life technologies, USA). The OGB was dissolved in dimethyl sulfoxide (DMSO) to make a 1×10^{-3} M solution. Furthermore, Pluronic F-127 (P-6867, Life technologies, USA) was dissolved in DMSO to make a 20% (w/v) solution. Both solutions were mixed at the same volume, followed by adding Neurobasal medium to make 10×10^{-6} M of OGB. The sample was treated with OGB solution and incubated at 37 °C for 30 min. Finally, cells were washed with fresh neurobasal media and stimulated by increasing the extracellular 50×10^{-3} M concentration of KCl.

3-2-5. Fixation and immunocytochemistry

We followed 3D cultured neuron immunostaining protocol as previously reported [46]. Cells were fixed in 4% paraformaldehyde and permeated with 1.0% Triton X-100 in PBS for 10 min. After these steps, cells were treated with a blocking solution of 10% (v/v) fetal bovine serum, 0.5% (v/v) Triton X-100, and 0.2% (w/v) gelatin in 0.1 M PBS at room temperature for 2 h. Primary antibodies against PSD95 (Novex, 1:200) and synaptophysin

(Chemicon, 1:200) were diluted in antibody solution: 5% (v/v) fetal bovine serum, 0.5% (v/v) Triton X-100, and 0.2% (wt/v) gelatin in 0.1 M PBS and incubated at 4 °C for 2 d. Species-specific secondary antibodies were incubated for 1 d at 4 °C. The nuclei were visualized with 2 μg mL −1 Hoechst (Molecular Probes, USA) staining for 2 h.

3-2-6. Image processing

We analyze the image data using the customized scripts in MATLAB (Mathworks, USA) for the neurite bundle figuration. First, the fluorescence images of the neural bundle were converted to grayscale. Second, each pixel was differentiated from the raw image along two perpendicular axes. Finally, the data was reconstructed with the matrix data sheet and quantified.

3-3. Results

3-3-1. Microfluidic device design for patterning ECM components in Matrigel

The microfluidic device was designed to align ECM components of the Matrigel with the micropillar arrays, as described in Figure 3-1 [77]. The microfluidic device allows the selective filling of each five distinct channels with different gels, cells, or media using four micropillar arrays. The micropillar to maintain the gel in the microfluidic device was designed into a triangular shape with 100 μm sides and 100 μm intervals. It provides avoiding the air interruption that frequently occurred in the previously suggested hexagonal shape and forming multilayered gel structure. The three central channels were filled first with Matrigel, while the remained channels were occupied with the media. Neurons were attached on the sidewall of Matrigel, where the hydrostatic pressure was applied. Liquid Matrigel at 4 °C was loaded into these channels and was placed in micropillar arrays. Additional medium was filled into the plastic reservoirs that resulted in the hydrostatic pressure on the Matrigel during the cross-linking process (Figure 3-1Ciii). The microfluidic device was kept in a 37 °C incubator for 3 h to allow the

organization of the cross-linking structure of the Matrigel.

To utilize our previous reports that gels were aligned along the flow line, we added a reservoir to generate consistent hydrostatic pressure across the whole device such that the flow would be uniformly distributed across the entire Matrigel filled section.

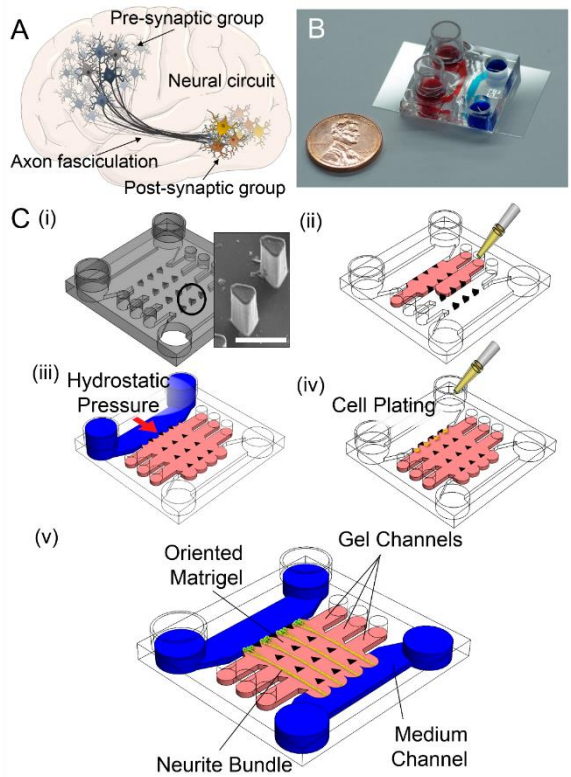

Figure 3-1. Three-dimensional (3D) neurite bundle formation in ECM hydrogel. (A) Structural feature of the neural circuit in the brain. A group of neurons form fasciculated bundles to reach its target post-synaptic cells. (B) Photograph of the 3D neural circuit device. (C) (i) Schematic of microfluidic device (box, SEM image of micro-pillar array. Scale bar, 200 μm), (ii) Gel loading step, (iii) 3D Matrigel alignment during gelation using hydrostatic pressure, (iv) Neuron plating step, and (v) Neurite bundle formation along flow direction in 3D Matrigel.

3-3-2. Engineering hydrogel cross-linking density

Immunofluorescence staining revealed that our method of using hydrostatic pressure on the Matrigel in the microfluidic device resulted in patterning the ECM components of the Matrigel. The density of collagen type IV as one of ECM components in the deformed Matrigel by the hydrostatic pressure was varied, while the density in the randomly cross-linked Matrigel without the pressure was uniform (Figure 3-2A). The density of deformed Matrigel in the microfluidic device showed that the compact gel and the sparse gel were alternated. The Matrigel has sparser cross-linking density distribution between two vertical micropillars.

The neurite growth in Matrigel also quantitatively imparts the Matrigel cross-linking density distribution. The neurites grown in randomly cross-linked Matrigel were distributed irregularly at every position and every height (Figure 3-2Aiii). However, neurites in the deformed Matrigel were converged within 70.0 ± 3.6 μm width as well as within 33.7 ± 1.6 μm height at the fixed cross-sectional view (Figure 3- B). In addition, the Matrigel cross-linking density distribution was different along the z -axis. Neurites in the patterned Matrigel were more grown at the center (z = +45 μm) of Matrigel than the top (z = +10 μm) or the bottom (z = +80 μm) at the fixed cross-section. On the

contrary, the distribution of neurite growth in randomly crosslinked Matrigel was constant at every height.

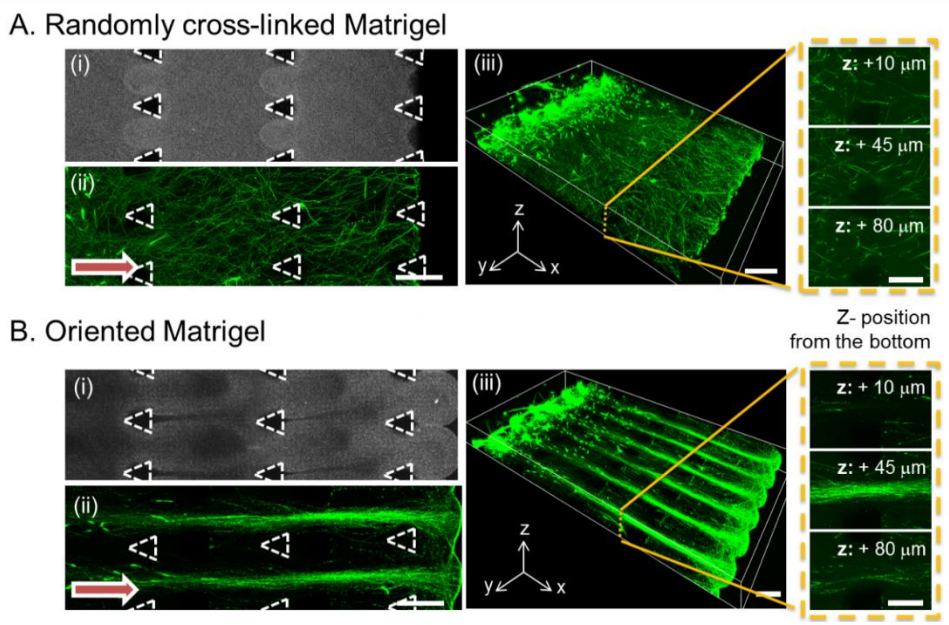

Figure 3-2. Comparison between random and deformed gel Matrigel. Collagen type IV, which is one of the main components in Matrigel, is visualized by anti-collagen immunostaining. Neurons are attached on the left side of the Matrigel. The red arrow indicates the direction of neurite propagation. A) (i) Randomly cross-linked Matrigel, Collagen type IV density distribution is evenly situated between micro-pillar arrays. (ii and iii) Neurites are spread through all directions including z-axis. B) Deformed Matrigel. Hydrostatic pressure was applied on the left side of device. (i) Collagen type IV distribution is deformed between micro-pillar arrays. (ii and iii) The scale bar indicates 200 μm (i-iii) and 100 μm (dashed box).

3-3-3. Factors to engineer the ECM components in Matrigel

To determine the factors that have infl uence on patterning of ECM components in Matrigel, we configured two types of design elements of the microfluidic device. First, the number of channels that were divided by micropillar structures was considered. To estimate its influence, ≈1–3 channels with varied intervals that allowed the same total of 1500 μm were manufactured (i.e., 1500 μm intervals in one channel experiment, 750 μm intervals between each channels in two channels, and 500 μm intervals between each channels in three channels, Figure 3-3A). We characterized the sparse Matrigel cross-linking density distribution by observing the length and the width of neural bundle formation. Both of these values were measured according to the number of channels at the fixed cross-section of 200 μm away from the last micropillar array as mentioned in the image processing section. The length of the emerged axon bundle was measured as 95.8 ± 3.7, 364.4 ± 24.5, and 757.6 ± 28.9 μm at ≈1–3 channels, respectively (Figure 3-3Aii). Also, the width from 1 to 3 channels was observed as 125.0 ± 4.2, 107.9 ± 3.1, and 70.0 ± 3.6 μm, respectively (Figure 3-3Aiii). When the number of the channels increased, the axon bundles were longer and more concentrated at the center of the two micropillar columns.

Another variable is the interval of the two micropillar columns. To experimentally evaluate the dependency of the micropillar interval on the Matrigel cross-linking density distribution, we also measured the length and width of axon bundles at three intervals of micropillar columns ranged from 50, 100, and 150 μm under the three channels (Figure 3-3B). We found that the length of the emerged axon bundle was increased while the width was decreased significantly ($p < 0.05$, $n = 5$). Respectively, the 50, 100, and 150 μm interval between two micropillar columns led to 873.9 ± 11.6, 757.6 ± 28.9, and 599.8 ± 19.3 μm length of axon bundle formation and 55.4 ± 2.5, 70.0 ± 3.6, and 90.8 ± 4.8 μm width (Figure 3-3B).

By using large reservoirs, hydrostatic pressure application allowed formation of novel structures such as radially focused axon bundles. This could not have been possible with the previous method and is an innovative step (Figure 3-4).

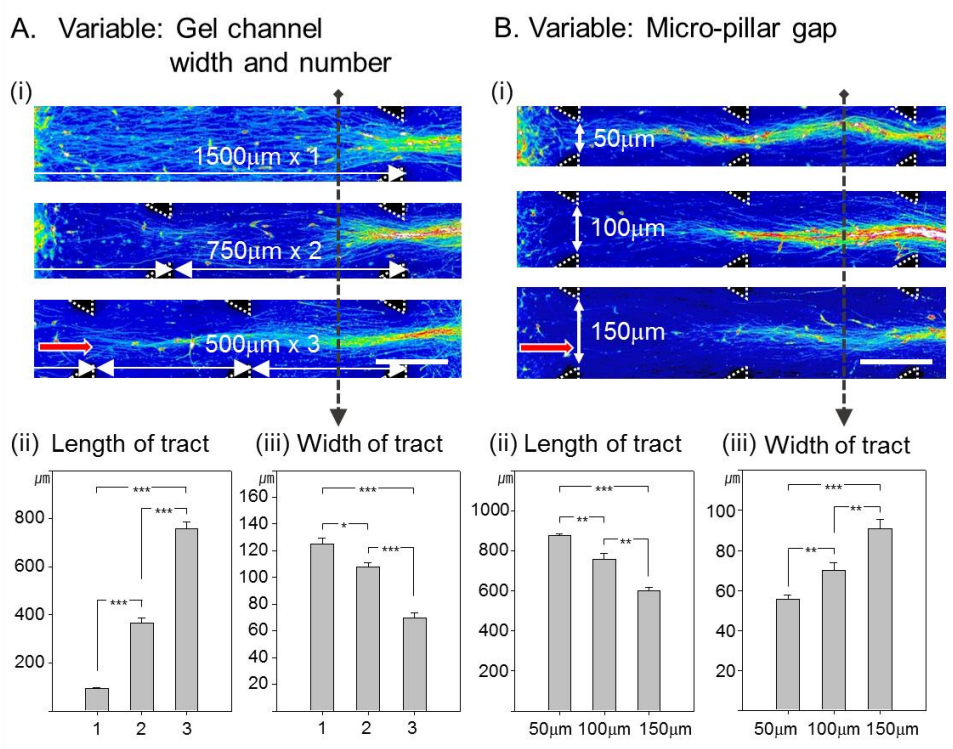
A. Variable: Gel channel width and number
(i)
1500µm x 1
750µm x 2
500µm x 3
(ii) Length of tract
(iii) Width of tract
µm
800
600
400
200
160
140
120
100
80
60
40
20
1
2
3
B. Variable: Micro-pillar gap
(i)
50µm
100µm
150µm
(ii) Length of tract
(iii) Width of tract
1000
50µm 100µm 150µm

Figure 3-3. Quantification of neurite bundle formation as a function of various design parameters. A) We quantified the neurite bundle length based on the difference of the number of channels and the channel width. The total width of the ECM channel for all cases was maintained at a constant value of 1500 μm. The bundle width was measured at the dashed line position. (i) Axon formation was visualized by Calcein AM staining. For a device with single, double, and triple gel channels, the axon bundles had (ii) longer and (iii) more slender characteristics as the gel channel number increased. B) We quantified the neurite bundle formation with various micro-pillar gap sizes. (i) Images of neurite bundles shape with difference gap size. Increasing the gap size leads to (ii) a decrease in axon bundle length, and (iii) an increase in axon bundle width. All samples are $n>5$. * <0.05, ** <0.01 and *** <0.001 paired student's t-test. The scale bar indicates 200 μm. Red arrow in the color map image indicates the direction of neurite bundle propagation.

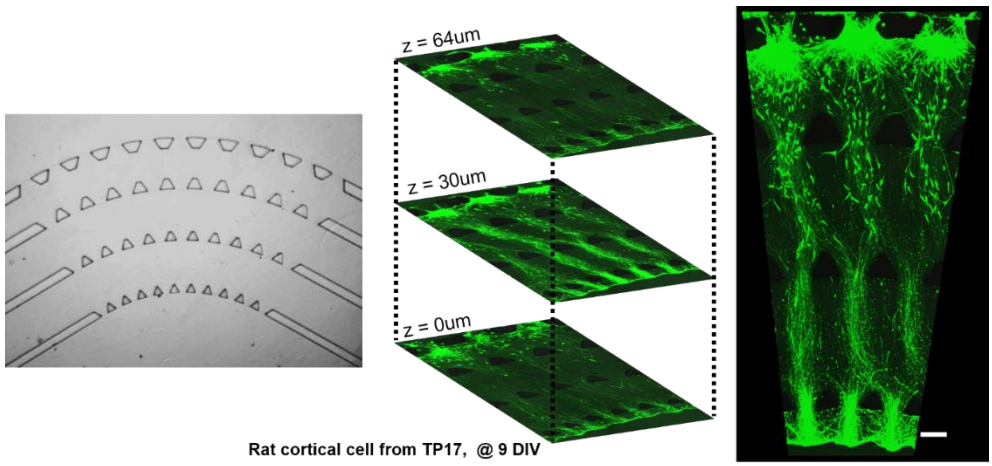

Figure 3-4. We introduced circular arc shape ECM hydrogel channels. After applying hydrostatic pressure, axon bundles grew in radial direction.

3-3-4. Neural bundle formation and axon fasciculation at long distance

Based on the microfluidic approach with the hydrostatic pressure, we established an *in vitro* model of neural bundle formation, axon fasciculation, and defasciculation that have the structural similarity of *in vivo* brain tissue. We confirmed these characterizations in our device by a live cell staining method. The microfluidic devices with three hydrogel channels and 100 μm intervals between two micropillar columns were used. Primary neurons were plated on the sidewall of the deformed Matrigel along the direction necessary to put the hydrostatic pressure on the gels. The plating concentration was optimized at 6×10^6 cells mL^{-1} as compared to other concentration values (Figure 3-5). With concentration less than 6 × 10 6 cells mL^{-1}, the axon was not capable of extending long distances, maintaining neurite alignment, and forming neural bundles. In contrast, axon fasciculation was dispersed at cell concentrations of more than 6 × 10 6 cells mL^{-1}. Neurites from the plated neurons were able to extend more than 1500 μm and axon fasciculation was formed after 6 days *in vitro* (DIV) (Figure 3-5B). Neurites grew into the deformed Matrigel at an average speed of 254.2 ± 6.5 μm d^{-1} ($p < 0.05$, n = 30, Figure 3-5B).

A. Cell viability optimization

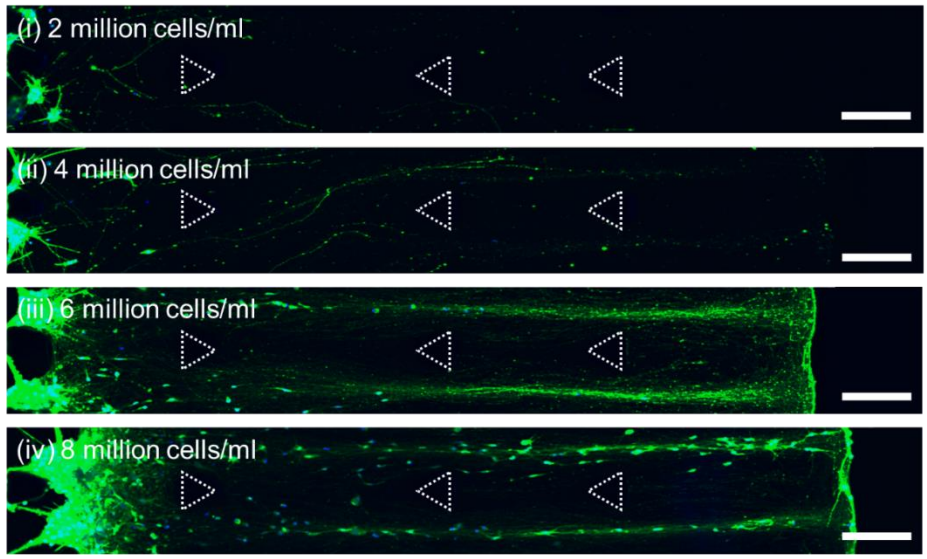

B. Neurite growth speed

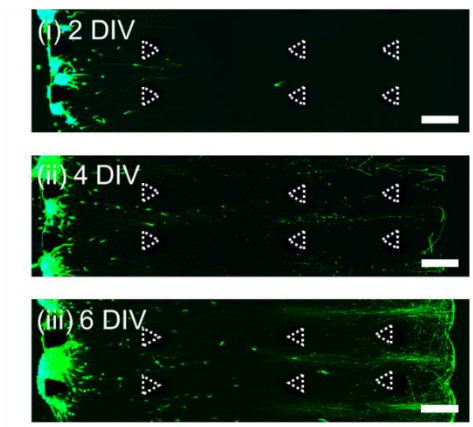

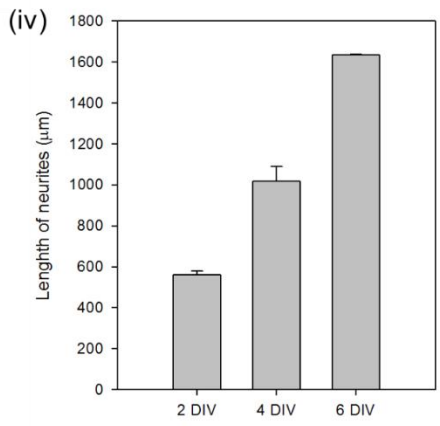

Figure 3-5. Characteristics of the bundle formation platform. A) Optimization of plated neuronal cell density. Fluorescence images of axons stained with calcein AM at 15 DIV. The plating concentration was optimized at 6×10^6 cells mL^{-1} as compared to other different concentration values. (i and ii) Cell density of less than 6×10^6 mL^{-1} did not have the capability of extending axons at long distances and maintaining neurite alignment as well as forming axon bundles. (iv) In contrast, axon fasciculations were dispersed at cell concentrations higher than 6×10^6 cells mL^{-1}. B) Optimization of neurites growth period. (i-iii) Neurites from the plated neurons were able to extend more than 1500 μm and axon fasciculation was formed after 6 days *in vitro*. (iv) Neurites grew into the deformed Matrigel at the average speed of 250 μm day^{-1} until 4 DIV. At 6 DIV, most neurites reached the opposite end of Matrigel (B. iv). (Scale bar: 200 μm.)

3-3-4. 3D Neural circuits

3D neural circuits were also developed in the patterned Matrigel with the hydrostatic pressure. he microfluidic device with an additional micropillar to fill in with gel-mixed cells was used (Figure 3-1C). We plated primary neurons on the sidewall of Matrigel as presynaptic neurons, and loaded gel-mixed neurons into the selective channel as postsynaptic neurons (Figure 3-6A). Two types of synaptic markers, the synaptophysin (presynaptic marker) and PSD95 (postsynaptic marker), were used to identify the synapse in the postsynaptic area (Figure 3-6B). We found that two types of markers were shown in close proximity (Figure 3-6B). The adjacent synaptic markers were located at the terminal of the neural bundle where axons were defasciculated. Moreover, we observed the signal transmissions from presynaptic neurons to post synaptic neurons by using a Ca^{2+} imaging technique (Figure 3-6C). When the saturated potassium chloride solution was inserted into the media channel to stimulate presynaptic neurons, the increased fluorescent levels passed through the axon of presynaptic neurons, and were then delivered into the neurite and the soma of postsynaptic neurons in a sequential way. This shows that the *in vitro* model with hydrostatic pressure on the Matrigel has a functional connection between presynaptic and postsynaptic neurons in

addition to structure similarity such as neural bundle formation and axon fasciculation.

The paper by Jang *et al.* was the first paper on this topic from our group [76]. That paper was focused on demonstrating that Matrigel can have aligned structure when gelled under slow flow and that can influence and guide axon growth. The main novelty described in this work is that we have demonstrated reliable formation of neural circuit in 3D containing axon fasciculation, defasciculation, and synapse development. We have characterized the neural circuit using electrical (Ca^{2+} signaling) and biochemical (immunostaining) means.

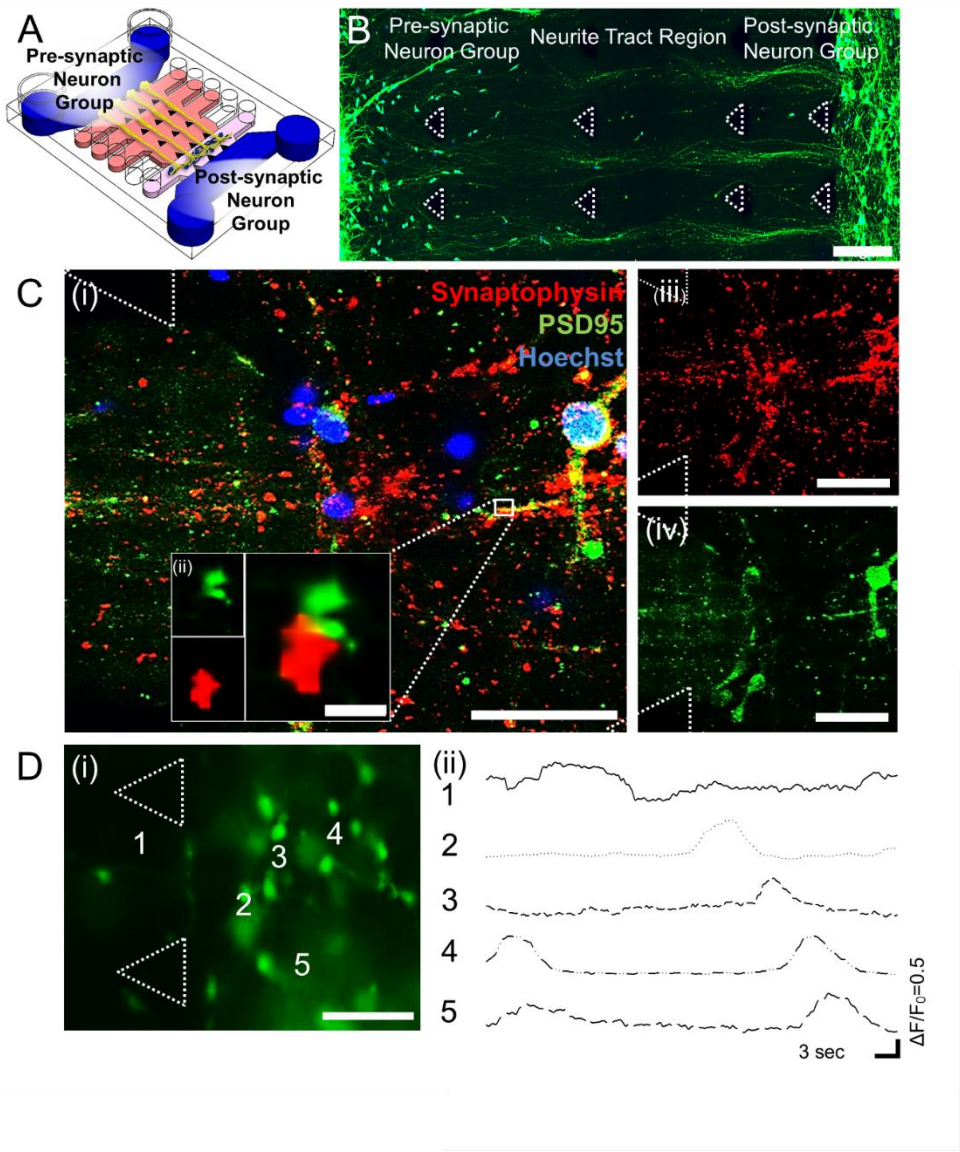
A
Pre-synaptic Neuron Group
Post-synaptic Neuron Group
B
Pre-synaptic Neuron Group
Neurite Tract Region
Post-synaptic Neuron Group
C
(i)
Synaptophysin
PSD95
Hoechst
(ii)
(iii)
(iv)
D
(i)
1
2
3
4
5
(ii)
1
2
3
4
5
3 sec
ΔF/F0=0.5

Figure 3-6. Three-dimensional neural circuit construction with fasciculate bundles. A) Schematic of aligned 3D neural circuit device. Pre-synaptic and post-synaptic neuron groups generated neural networks parallel with the deformed ECM components. B) Neural circuit composed of pre-synaptic neuron group, neurite bundle region, and post-synaptic neuron group. The neural circuit was visualized with calcein AM and Hoechst. C) Synapses at post-synaptic neuron group area. Neuronal cells were immunostained with a pre-synaptic marker (synaptophysin, red) and post-synaptic marker (PSD95, green) at 12 DIV. (ii)Synapses were detected by fluorescence imaging with pre-synaptic and post-synaptic marker signals being adjacent to one another. D) Intracellular calcium live imaging of a three-dimensional neuronal circuit. (i) Fluorescence image of BAPTA-1 AM-loaded 3D neuronal network at 14 DIV. Numbers indicate the change point of fluorescent intensity. (ii) The fluorescent intensity represents the intracellular calcium ion concentration. As shown in $\Delta F/F_0$ graph, the fluorescence level spikes starting from neurite bundle (1) to post-synaptic neurons (2 to 5). The scale bar indicates 200 μm (B), 50 μm (C. i, iii, iv), 1 μm (C. ii) and 100 μm (D).

3-4. Discussion

There are not much previous works on alignment of molecules in polymerizing gels due to hydrostatic pressure or shear stress. A paper by Odawara *et al.* is the most relevant work where collagen I prepolymer was flowed while gelling at the same time (ECM itself was flowing compared to media flowing through the ECM network for our work) to generate alignment [75]. In our previous work by Jang *et al.*, the device was tilted at 90° while polymerizing/cross-linking Matrigel [76]. Using this method, the magnitude and direction of pressure applied to the Matrigel could not be controlled precisely.

In this work, we placed large reservoirs on one side of the device to generate reproducible and quantifiable hydrostatic pressure. The best condition for alignment was when the hydrostatic pressure was about 12 mmH_2O. If the hydrostatic pressure is lower than 12 mmH_2O, ECM alignment was not clearly evident. Matrigel was damaged when pressure was higher.

We have performed detailed characterization of the process and quantification of neuron culture. For example, the device design optimization, optimization of cell number, post shape, interpost distance, and neurite

extension, and quantification at various DIV. Due to our additional analysis and optimization (by inserting groups of posts in the middle of the gel), we were able to form fasciculated axon bundles in the devices. Such improvement will be valuable in future work where oligodendrocytes will be cocultured to form myelinated neural circuits.

3-5. Summary

A new *in vitro* model that has the structural similarity with intact *in vivo* brain tissue was established in a microfluidic chip by regulating the cross-linking structures of the ECM components in Matrigel. The Matrigel in the microfluidic device displays cross-linking density distribution patterns when the hydrostatic pressure was applied on the Matrigel during the gelation process. The density of the patterns, either dense or sparse, is decided by the geometry of the micropillar and the number of gel channels. Axons grew as neural bundles formed with fasciculation and defasciculation in 3D deformed Matrigel, which is normally observed in the brain. Furthermore, 3D neural circuits with visualized synapses were also formed and have the ability to propagate sequentially from neural bundles in presynaptic neurons to postsynaptic neurons.

This microfluidic device can be introduced into synapse and neural circuit formation/maturation research with a genetic, electric, and biochemical gradient. Additionally, by locating more than two neural circuits in this microfluidic device in series or in reverse, we can produce a complex neural circuit. Moreover, this proposed microfluidic device can produce myelination and neuromuscular junction research by coculture. Therefore, this new

developed microfluidic platform can be used in various neurosciences and also neurodisorder drug research.

Chapter 4. A Low Permeability Microfluidic Blood-Brain Barrier Platform with Direct Contact between Perfusable Vascular Network and Astrocytes

---

Published in Scientific Reports, 2017, 7, 8083 (78)

4-1. Introduction

The blood-brain barrier (BBB) is a part of the neurovascular unit (NVU) that exist as a complex of blood vessels, astrocytes and neurons [79, 80]. Structurally, the BBB has a direct interface via astrocytic endfeet anchored in the basal lamina of the adjacent capillary wall (Fig. 4-1A) [81, 82]. At the interface, many transport channel proteins, such as aquaporin 4, facilitate exchange between the astrocytic endfeet and the capillary network [83]. With the complex network of transport channels between the astrocytes and the capillary network, the BBB selectively restricts exchange of blood-bound substrates between the brain and the rest of the circulatory system [84, 85].

As the BBB is a major obstacle to pharmacologically active substances when targeting the brain, it is the subject of much experimentation and study

with regards to CNS drug delivery. Conventional experimentation is generally done *in vivo* on lab animals, which are both expensive and difficult in terms of animal upkeep and purchasing costs, equipment, reagents, and observation [86]. Due to the high entry barrier and costs of current conventional *in vivo* based modeling, the development of a suitable *in vitro* model platform is urgently needed. Transwell platforms, capable of co-culturing segregated cells in micropore membrane separated compartments, are one of the representative platforms for disease modeling and drug screening [87, 88, 89, 90]. Booth *et al*. proposed a microfluidic device incorporating Transwell like micron pores into an integrated *in vitro* BBB platform [91, 92, 93, 94]. Further studies have also established the capability of generating chemical gradients and cell patterning within membrane integrated microfluidic devices [95, 96]. Recently, Adriani *et al*. proposed a platform of seeding three-dimensional tissue cultures in a ECM hydrogel to produce a structural *in vitro* BBB model [97, 98]. All of the aforementioned BBB platforms are limited by the inability to generate *in vivo* like direct interfaces between astrocytes and a vascular network, do not exhibit the characteristic low permeability of the vascular networks, and are unable to independently treat the inner and outer lumen of the vascular network independently.

The proposed platform employs a system of two separate media

microchannels to independently emulate highly localized internal and external vascular microenvironments. The two media microchannels, designated as the Vascular Channel (VC) and the Neural Channel (NC), supply their respective co-culture tissues independently of one another, and can serve as the microenvironment of the outside and the inside of the BBB respectively. The VC connects to the inner lumen of the vascular network, while the NC supplies the neural cells directly attached to the vascular network. The Vascular Network Channel (VNC) generated by this platform exhibits direct contact between neural and vascular tissues and a corresponding low permeability characteristic of *in vivo* BBB (Fig. 4-1A), suggesting that the dual-channel co-culture method has broad applications in vascular and neural tissue network construction.

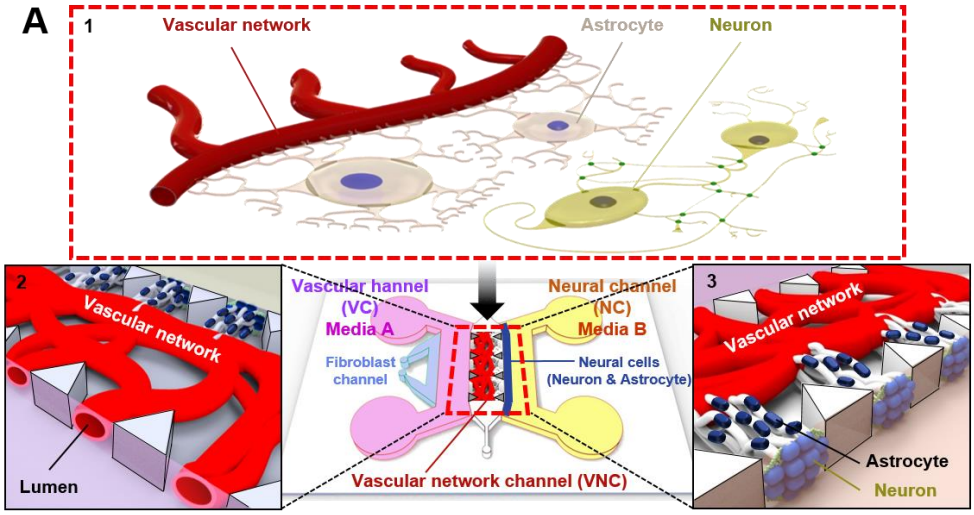
A
1
Vascular network
Astrocyte
Neuron
2
Vascular network
Lumen
Vascular hannel
(VC)
Media A
Neural channel
(NC)
Media B
Fibroblast
channel
Neural cells
(Neuron & Astrocyte)
Vascular network channel (VNC)
3
Vascular network
Astrocyte
Neuron

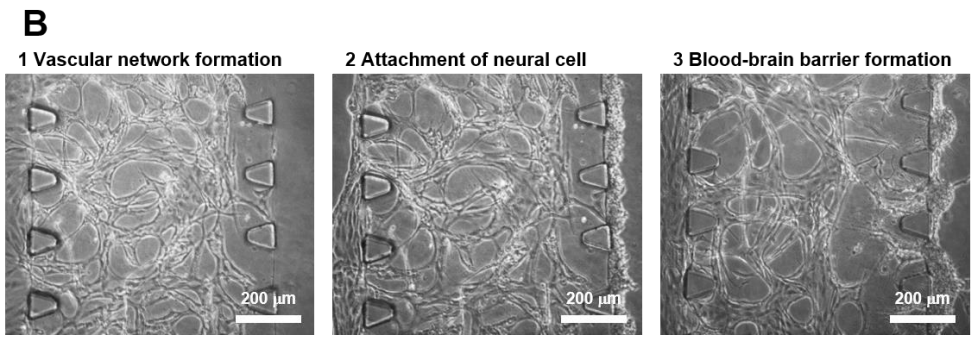
B
1 Vascular network formation
2 Attachment of neural cell
3 Blood-brain barrier formation
200 μm
200 μm
200 μm

Figure 4-1. Microfluidic platform for neurovascular unit (NVU) including blood-brain barrier (BBB). (A) The neurovascular unit includes a highly selectively permeable vascular feature called the blood-brain barrier which is composed of a complex network of capillaries and astrocytes. The astrocytes are directly interfaced with the capillaries through astrocytic endfeet, which anchor the neurons to the vascular network. Adjacent to the BBB are neural circuits composed of synaptic neural networks. (1) Proposed in vitro 3D NVU platform. The in vitro NVU platform consists of an engineered BBB co-culture of astrocytes integrated into a vascular network, and a neuronal network "interior" to the BBB. The vascular network component is generated first in the dedicated Vascular Network Channel (VNC). As the vascular network forms, individual lumens form in the area between each posts on the Vascular Channel (VC) for VNC bound media. Neural cells are applied to the Neural Channel side of the nascent vascular network. ("Neural channel", NC) of the VNC (2, 3). (B) The process of platform generation. The perfusable vascular network is formed over a 3-day period via vasculogenesis protocol. The lumen of the vascular network is not yet open to the VC at this time (1). A suspension of freshly isolated neurons and astrocytes is loaded into the NC side of the VNC by applying the cell suspension to the NC media channel and tilting the device in such a way that flows the neurons and astrocytes towards

the VNC posts and causes them to settle on the VNC/NC border posts (2). The VC and NC media channels are supplied with their respective optimized media, allowing for the formation of the BBB tissue within 5 to 7 days (3).

4-2. Materials and Methods

4-2-1. Microfluidic device fabrication

Microfluidic devices are fabricated by soft lithography, which utilizes a master device to create multiple soft molds. The master with embossed structure of negative photoresist SU-8 (MicroChem) was developed by photolithography on a 4-inch silicon wafer. A 10:1 (w/w) Polydimethylsiloxane (PDMS, Sylgard 184, Dow Corning) and curing agent was poured on the master and degassed in a vacuum chamber for removing bubbles and thermally cured to obtain a negative replica molds. Using biopsy punch (6 mm) and sharpened blunt syringe needle (0.5 mm), medium reservoirs and hydrogel injection parts were punched out. The PDMS molds and glass coverslip, which are treated with oxygen plasma to form covalent bonding between them, were cleaned with residue-free tape and nitrogen gas air gun. After bonding, the device was followed by the incubation in an 80 °C dry oven at least 48 hours to maintain hydrophobic condition. The devices were sterilized by UV irradiation before experiment.

4-2-2. Cell culture

Human umbilical vein endothelial cells (HUVECs, Lonza) were cultured in endothelial basal medium-2 supplemented with EGM-2 SingleQuots Kit (EGM-2, Lonza) and passages 3 to 5 were used for the experiments. Normal human lung fibroblasts (LFs, Lonza) were cultured in fibroblast basal medium supplemented with FGM-2 BulletKit (FGM-2, Lonza) and passages 5 to 7 were used for the experiments. In terms of HUVECs, cells were cultured for experiments before reaching 80 to 90% of confluent. All cells were incubated in a humidified 5% CO2 atmosphere and at 37 °C.

4-2-3. Cell plating for vasculogenesis in the microfluidic device

Fibrinogen solution was made by dissolving bovine fibrinogen (10 mg/ml, F 8630, Sigma-Aldrich) in Dulbecco's phosphate-buffered saline (DPBS, Hyclone) and filter sterilized (0.22 μm pore). Then, Mixing with aprotinin (0.15 U/mL, Sigma-Aldrich). HUVECs and LFs, which are detached from the cell culture dishes by treating 0.25% Trypsin-EDTA (Hyclone), were centrifuged and suspended at concentration of 6.7 million cells per ml in EGM-2 medium. The cell suspensions are mixed with the fibrinogen solution at a ratio of 3:1 to yield a final concentration of HUVECs and LFs as 5 million

cells per ml, respectively. The mixtures with thrombin (0.5 U/ml, T4648, Sigma-Aldrich) were injected into the center hydrogel micro-channel and side micro-hydrogel channel. After 5 minutes at room temperature, the gel mixtures formed structures and the upper reservoirs in each device were filled with culture medium (EGM-2) and aspirated gently at the lower reservoirs to make the hydrophobic medium micro-channel. Following filling evenly rest of reservoirs with the medium, the devices were incubated at 37 °C and 5% CO2. The culture medium was changed into fresh EGM-2 culture medium every 48 hours.

4-2-4. Cortex neural cell preparation and plating in the microfluidic device

We used Sprague-Dawley embryonic rat (E17) for preparing rat cortical neurons. The rat cortices in trypsin-EDTA solution (Gibco, USA) were incubated at 37 °C water-bath for 12 min. After incubating, the trypsin-EDTA solution took away, and Dulbecco's modified Eagle's medium (DMEM, Gibco, USA) with 10% Fetal Bovine Serum was supplied to stop trypsin reaction. The DMEM solution was removed, and Neurobasal medium (Invitrogen) with 2% B27 supplement (Invitrogen, USA), 0.25% GlutaMax (Invitrogen), and 1% penicillin–streptomycin (Invitrogen, USA) was supplied.

The cortices were cut into small pieces with 1 ml and 200 μl pipet tip. After this process, the cell suspension was made and filtered by cell strainer. The cell suspension is diluted with neurobasal medium to required concentration, 8 million cells per ml. The 50 μL cell suspension was put into microfluidic device. To settle the

cells down to the surface of fibrin hydrogel, the microfluidic device was tilted at 90° degrees in 37 °C incubator for 30 min. For VEGF-A test, VEGF-A was added to Neurobasal medium so that the concentration of VEGF-A was 100 ng/ml. All acquisition procedures of biological samples were approved by the Institutional Animal Care and Use Committee of the Seoul National University, and all experiments were conducted in accordance with the relevant guidelines and regulations set by the Committee.

4-2-5. Immunostaining

Samples were washed at least twice with PBS and fixed in 4% paraformaldehyde (PFA, Thermo) for 15 minutes at room temperature. After fixation, cells were permeabilized with 0.15% triton-X 100 (Sigma-Aldrich) for 20 minutes at room temperature. Samples were then treated with 3% bovine serum albumin (BSA, Sigma-Aldrich) to minimize nonspecific

antibody binding and Hoechst 33342 in PBS to stain nuclear for 1 hour at room temperature. After washing with PBS, samples were stained with Alexa Fluor(R) 488 anti-mouse CD31 antibody (monoclonal, Cat. No. 303110, diluted 1:200, Biolegend) as an endothelial cell marker, Alexa Fluor(R) 647 anti-GFAP antibody (monoclonal, Cat. No. 560298, diluted 1: 200, BD phamigen) and anti-synaptophysin antibody (Polyclonal, Cat. No. ab32594, diluted 1: 200, Abcam).

4-2-6. Synapse number measurement

Synapse images were determined by staining for synaptophysin. Images were taken using a confocal microscope (Olympus FV1000). IMARIS (Bitplane, Switzerland) was used for reconstructing three dimensional images. The cells between micro-posts were analyzed. Using the Spot function of IMARIS, the nucleus of cell above 4.5 μm diameter and the synaptophysin above 1.0 μm diameter were counted.

4-2-7. Area of vascular network and astrocytes measurement

The 3D reconstructions and cross-sections of the vascular network and

astrocytes were determined by using a confocal microscope (Olympus FV1000). Images were analyzed by imageJ. To quantify the area of vascular network, Z-projections of the 3D stacks were obtained and then each image was masked from the backgrounds before measurement.

4-2-8. Permeability coefficient measurement

A fluorescence image of FITC-dextran diffusing across vascular network was analyzed for calculating the permeability coefficient. After removing all media from medium reservoirs, 50 μl of 20 kDa FITC-dextran solution was flowed into the VC. 70 kDa FITC-dextran solution was treated as the same way. For observation of the permeability of the vascular network, an inverted epifluorescence microscope (Olympus IX81) was used. Images were taken in every 25 second interval. The equation for calculating the permeability coefficient is derived from previous study.

4-2-9. Statistical analysis

All data were plotted as mean ± SEM. The student's t-test is used statistically to analyze the different datasets.

4-3. Results

4-3-1. The effect of medium in the neural cell culture

While typical neuron cultures are supplied with serum-free B27 (NBMB27) neurobasal media, the necessity to introduce serum into the system for the sake of the co-cultured endothelial cells warranted further investigation [30, 99]. Furthermore, as the inclusion of serum in neurobasal media is atypical, it was paramount to determine the potential effects of serum in neural tissue, prior to use. In order to quantitatively assess the effects of serum in neuron culture medium, several characteristics of neuron morphology were selected and observed in an experimental scheme. The ability to form synaptic connections between neurons, as both an objectively quantifiable variable and as a vital characteristic of neurons, served as a suitable candidate for observation. Relative differences in synaptic connections between neurons in serum-free control and various serum containing intervention group media in neuron cultures were quantified and assessed [100, 101]. Neural cells of cortex origin were attached to fibrin hydrogels within test platform microfluidic chips and mono-cultured in different growth media, supplied through both VC and NC channels (Fig. 4-

2A). The supplied media were formulated in the following categories: Neurobasal media (NBM) with FBS; Neurobasal media without FBS; and endothelial growth medium (EGM). For each experimental group, the ratio of synaptic connections to the number of neurons in the cell mass area between microposts (Fig. 4-2B) were taken as a metric. The experimental media formulations are as follows: NBM with B27 supplement (NBMB27); NBM with 2% FBS (NBMFBS); EGM with 2% FBS. B27 was determined to serve an analogous function in NBM as FBS, and therefore no medium was tested with both B27 and FBS. The resulting data was as follows: NBMB27 8.60 ± 1.50; NBMFBS, 9.20 ± 0.84; EGM, 3.49 ± 0.37. Both NBMB27 and NBMFBS treatment groups exhibited near equivalent synaptic connection per neuron values, while the EGM treatment group was observed to have much lower values (Fig. 4-2C). As demonstrated by the equivalent per-cell synaptic generation ratio values between NBMB27 and NBMFBS, it was determined that FBS was suitable for use in the proposed co-culture platform.

In addition to diminished synaptic generation, EGM cultured astrocytes were observed to migrate into the adjacent blank ECM (fibrin hydrogel). Neither NBMB27 nor NBMFBS cultured neurons exhibited migration of this nature. As the inclusion of VEGF in EGM is one major difference between EGM and NBM, and it has been reported that VEGF-A has been associated

with the increased proliferation and migration of astrocytes, it was postulated that the VEGF in EGM was the cause of the observed EGM cultured astrocyte migration [102, 103].

To confirm the pro-proliferative and pro-migratory effect of VEGF-A on neurons, separate experimental schemes of neurons in NBMB27 with VEGF-A, and NBMFBS with VEGF-A were cultured. In both cases, neurons cultured entirely in media supplemented with VEGF-A exhibited both increased proliferation and a very brief period of migratory behavior compared to the baseline of VEGF-A absent cultures. Increased proliferation was monitored by means of GFAP stain imaging (Figure 4-3). When a gradient of VEGF was established in further co-culture experimentation which will be addressed in the next section, astrocytic migration was observed in drastically higher degrees than in co-cultures with a uniform VEGF concentration (Figure 4-4 and Figure 4-5).

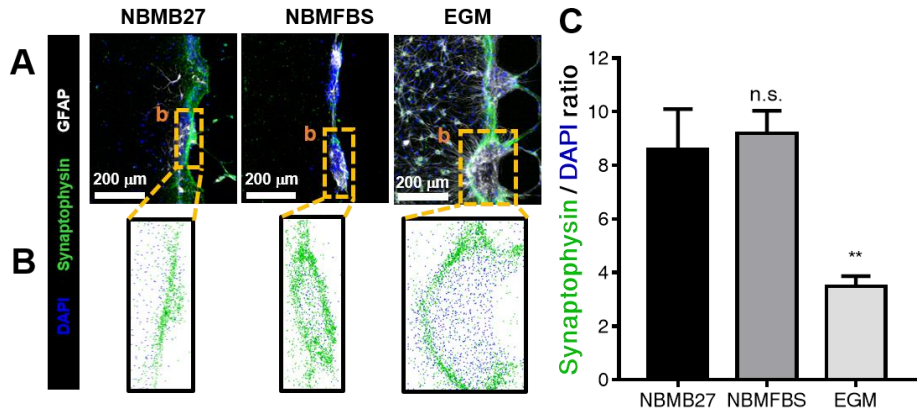

Figure 4-2. Comparison of three neuron cultures in NBMB27, NBMFBS, and EGM for assessing the effect of FBS in neural cultures. (A) Immunostained images of each experimental medium culture. (B) The total number of nuclei and synapses identified in each culture. As the neurons were grown in a mass against the fibrin hydrogel wall and do not migrate, synaptic connections were measured at the cell mass. (C) The per neuron average of synaptic connections value for NBMFBS was found to be similar to that of cultures grown in NBMB27 control. EGM supplied neuronal cultures show a drastic decrease in synaptic connectivity. All data show mean ± SEM. Statistical analysis student's t-test. $^{**}p < 0.01$. 12 ROI for each condition were used for analysis.

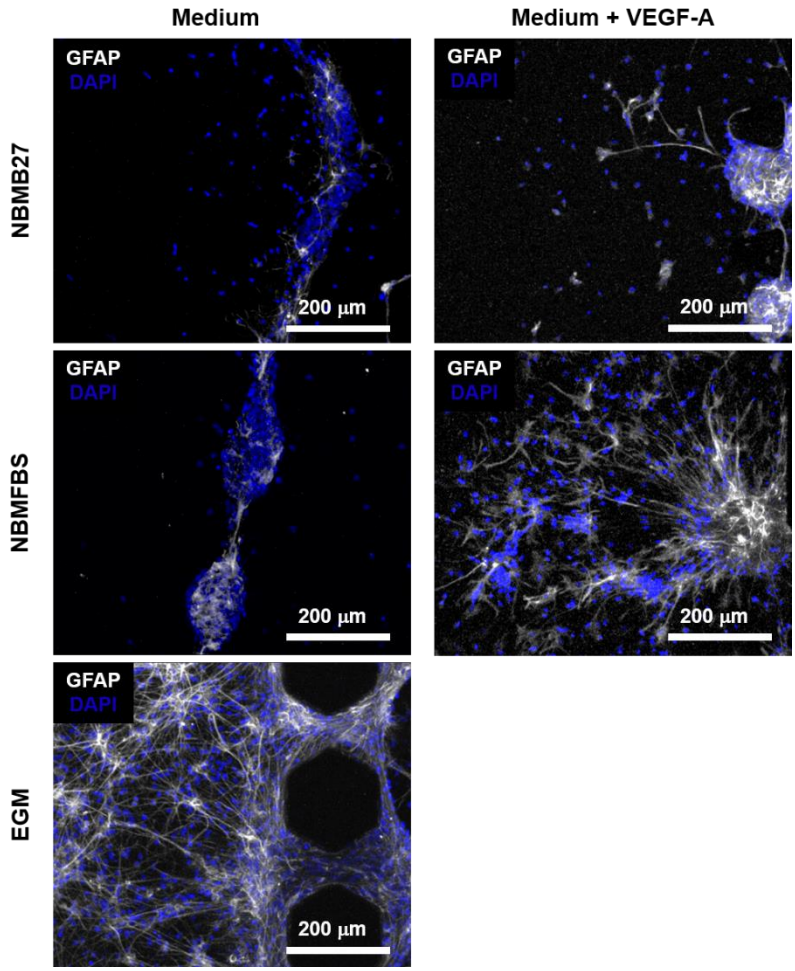

Figure 4-3. The effect of VEGF-A on the proliferation of astrocytes. Unlike EGM, NBMB27 and NBMFBS do not have VEGF. Astrocytes also proliferate prominently in EGM condition but less proliferate in NBMB27 condition and NBMFBS condition. On the other hand, the proliferation of astrocytes is observed when VEGF-A (100 ng/ml) is added to NBMB27 or NBMFBS.

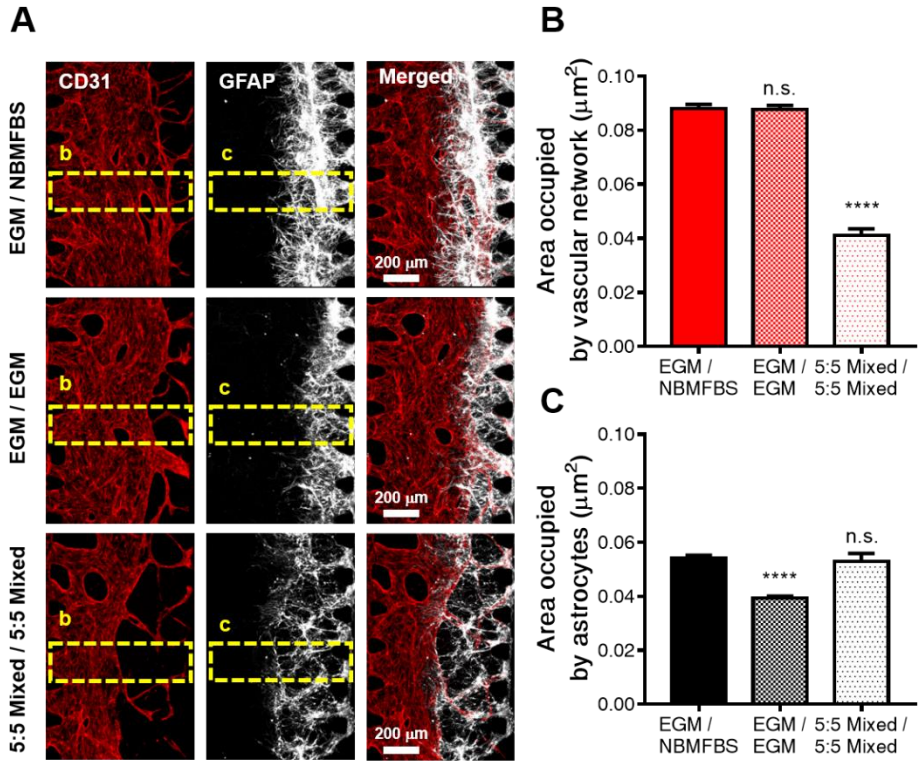
A
CD31
GFAP
Merged
EGM / NBMFBS
EGM / EGM
5:5 Mixed / 5:5 Mixed
b
c
200 µm
B
Area occupied by vascular network (µm²)
0.10
0.08
0.06
0.04
0.02
0.00
n.s.
****
EGM / NBMFBS
EGM / EGM
5:5 Mixed / 5:5 Mixed
C
Area occupied by astrocytes (µm²)
0.10
0.08
0.06
0.04
0.02
0.00
****
n.s.
EGM / NBMFBS
EGM / EGM
5:5 Mixed / 5:5 Mixed

Figure 4-4. Comparison of vascular network and astrocyte areas in experimental medium co-culture conditions. (A) CD31 stained vascular networks shown in red, GFAP stained astrocytes shown in white for all three experimental medium compositions (annotated in VC/NC supplied channels): EGM/NBMFBS; EGM/EGM; 5:5 mix of NBMFBS:EGM for both channels. Vascular network bound media was supplied through the Vascular Channel (VC), and neuron bound media was supplied through the Neural Channel (NC). In the presence of EGM, astrocytes exhibited increased proliferation and migratory behavior. Astrocytes were observed to migrate from the initial neural cell suspension injection zone to the border of the vascular network. (B) Average area occupied by the vascular network between a pair of parallel microposts. In cultures where VC was supplied with ECM, (EGM/NBMFBS and EGM/EGM), vascular network areas were roughly equivalent. (C) Average area occupied by astrocytes between a pair of parallel microposts. Cultures supplied with NBMFBS via the NC, exhibited the highest astrocytic areas. All data show mean ± SEM. Statistical analysis student's t-test ****$p < 0.0001$. 51 ROI for each condition were used for analysis.

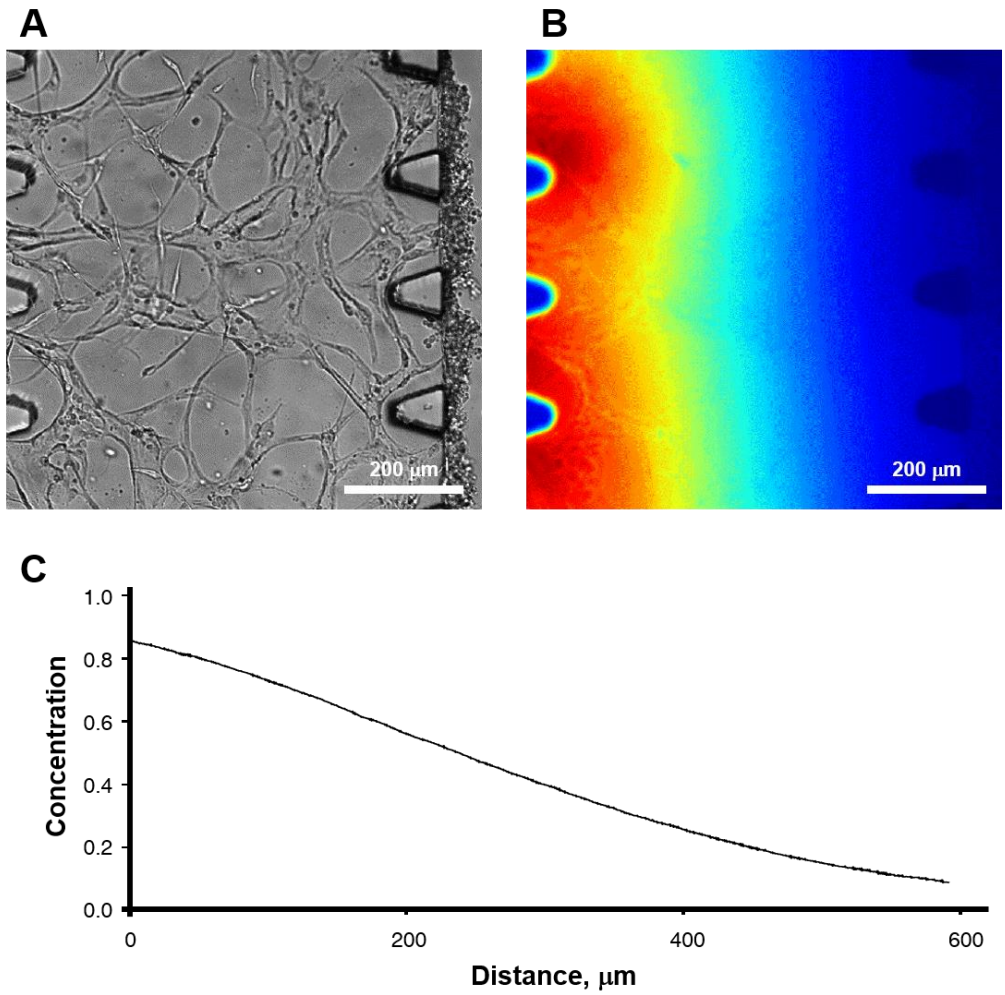
A
200 μm
B
200 μm
C
Concentration
1.0
0.8
0.6
0.4
0.2
0.0
0
200
400
600
Distance, μm

Figure 4-5. Linear gradient inside fibrin hydrogel before lumen of vascular network opens to medium channel. (A) The vascular network was cultured in the fibrin hydrogel for 3 days. The lumen of the vascular network is still not connected to the medium channel. Therefore, the wall surface of the fibrin hydrogel is still maintained. At this point, neural cells are attached to one side of the fibrin hydrogel. FITC-dextran was injected into the medium channel opposite to the neural cell. (B) At this time, FITC-dextran (20 kDa) gradient across the fibrin hydrogel is not affected by the vascular network. FITC-dextran shows a linear gradient in the fibrin hydrogel. (C) Diffusion profile inside of fibrin hydrogel. This diffusion profile was measured 10 minutes after FITC-dextran injection.

4-3-2. The effect of medium in the co-culture with vascular network and neural cells

As it was with the investigating the impact of new supplementary substrates in neural cultures, the same consideration was warranted for endothelial cells. To test the effect of NBMFBS on the vascular network, a co-suspension of HUVEC and fibroblasts in fibrin were loaded first on the VC side of the device. Vascular networks formed from the seeded HUVEC and LF after three days of incubation, although the lumen of the network did not open towards the media channel at this time. Neural cells are then seeded on the surface of the fibrin hydrogel surface into the neuron growth chamber (Fig. 4-1B). At this time, the vascular network is displaced away from the NC, and the vascular lumen is connected to the VC. Astrocytes have also been observed migrating towards the vascular network, stopping only when contact with the EC is made. In all cases, astrocytic migration was observed to stop at the vascular network (Fig. 4-4A and Fig. 4-6). ZO-1 immunostaining was used to confirm the presence of BBB tight junctions along the interface regions between astrocytes and the vascular network (Fig. 4-7D) [104].

At all tested concentrations, in the presence of NBMFBS, vascular networks were observed to contract and narrow. Conversely, the presence of EGM was observed to preserve typical vascular network morphology. The

resulting measurements per media composition are as follows (medium in the VC/medium in the NC): EGM/NBMFBS, 0.0881 ± 0.0015 μm^2; EGM/EGM, 0.0876 ± 0.0016 μm^2; 5:5 mixed/5:5 mixed, 0.0411 ± 0.0025 μm^2 (Fig. 4-4B). Results confirm that EGM is indeed the superior growth medium for optimal vascular network growth and maintenance. Different media conditions were also observed to influence the degree of astrocytic migration. To quantify astrocytic migration under the tested media composition profiles, the area of astrocyte migration was observed in each experimental group. The observed astrocytic migratory areas by media composition are as follows (medium in the VC/medium in the NC) EGM/NBMFBS, 0.0542 ± 0.0010 μm^2; EGM/EGM, 0.0393 ± 0.0008 μm^2; 5:5 mixed/5:5 mixed, 0.0529 ± 0.0029 μm^2 (Fig. 4-4C). The data suggests that NBMFBS supplied to the NC results in a larger area of astrocytic migration than when EGM is supplied to NC. To reiterate, the supply of EGM to the VC appears to aid in maintaining good vascular morphology, and the supply of NBMFBS to the NC appears to promote astrocytic migration. In co-cultures supplied with NBMFBS to the NC and EGM to the VC, astrocytic and vascular network overlap was the highest amongst all other tested co-cultures. Given the VEGF-A mediated promotion of neuron proliferation and migration as observed previously, it was hypothesized that the generation of a VEGF gradient within the fibrin

hydrogel may have played a part in the increased vascular network and astrocytic overlap. To confirm the hypothesis, co-cultures supplied with media containing VEGF-A on one side through the VC, and VEGF-A absent media through the NC were compared with co-cultures supplied with exclusively VEGF-A supplemented and VEGF-A absent media. Co-cultures with a VEGF-A gradient exhibited a much higher degree of vascular/astrocytic overlap than in non-gradient co-cultures. In order to visualize the gradient of VEGF-A side media with a VEGF-A/nonVEGF-A medium supplied co-culture, FITC-dextran was added to the VC prior to the opening of the vascular lumen to the channel. A linear gradient of FITC-dextran was observed in the fibrin hydrogel originating from the VEGF supplied media channel (Fig. 4-5).

Due to the importance of confirming the direct contact between astrocytes and the vascular network, overlap areas were imaged via immunofluorescence staining high-resolution confocal microscopy. Because of the three dimensional nature of the platform, it was difficult to confirm direct contact between astrocytes and the vascular network from top-down imaging alone, as tissue formation may have occupied the same area from a top down view, but may have grown at different elevations of the channel and thus did not physically come into contact. Therefore, neurovascular interfaces

were visually confirmed through imaging on a two-axis cross-sectional basis to ensure both top-down and lateral contact. (Fig. 4-7 and Fig. 4-8). This phenomenon was observed in every medium condition (Fig. 4-9). In addition, aquaporin 4 channels were observed only where direct neurovascular contacts formed. (Fig. 4-10).

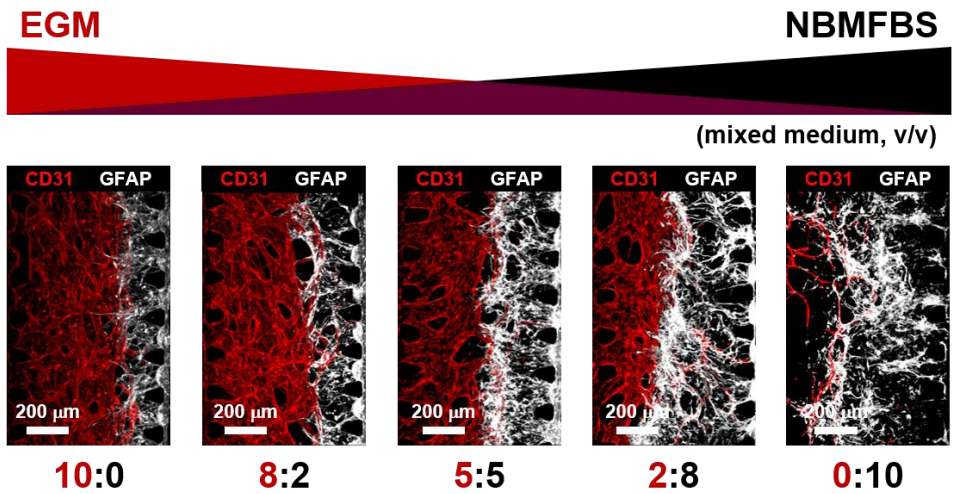

Figure 4-6. Area difference of vascular network and astrocytes under various conditions. In this experiment, the medium in VC and NC is the same. Reduced amount of EGM in the medium micro-channels makes smaller area of the vascular network. However, reduced amount of EGM in the medium micro-channels makes the larger area of the astrocytes.

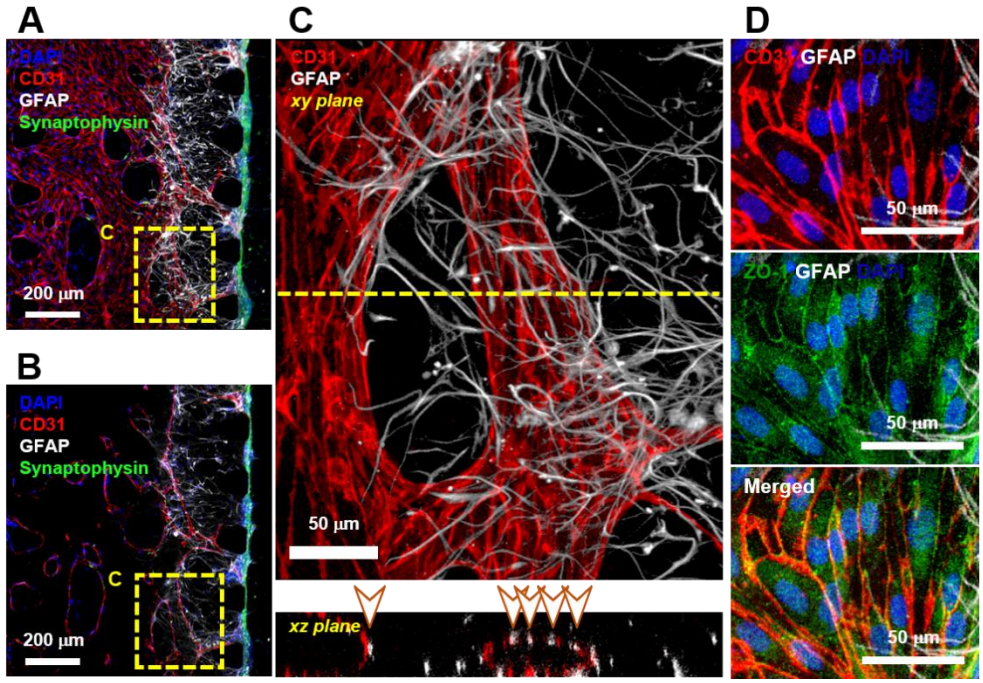
A
DAPI
CD31
GFAP
Synaptophysin
C
200 μm
B
DAPI
CD31
GFAP
Synaptophysin
C
200 μm
C
CD31
GFAP
xy plane
50 μm
xz plane
D
CD31 GFAP DAPI
50 μm
ZO-1 GFAP DAPI
50 μm
Merged
50 μm

Figure 4-7. Immunostained imaging of the vascular network - astrocyte interface. (A) Astrocytic migration from the NC side neuron-astrocyte loading suspension follows the VEGF gradient towards the VC, and stops after directly interfacing with the vascular network. The neuronal synaptic network is clustered to the right of the fibrin gel, adjacent to the astrocyte-vascular interface. (B) An intermediate section layer of the NVU platform. Vascular network lumens form between each VC facing micropost, with each opening occupying the space of the entire post gap. The vascular network is perfusable from the VC, but is not connected to the NC. (C) Imaging of the direct vascular network-astrocyte interface. Confocal microscopy confirmed direct contact on two axes, with contact points indicated in the xz plane render via arrow points. (D) Vascular network - astrocyte contact confirmed through immunostaining for ZO-1 tight junction protein expression by CD31 positive endothelial cells.

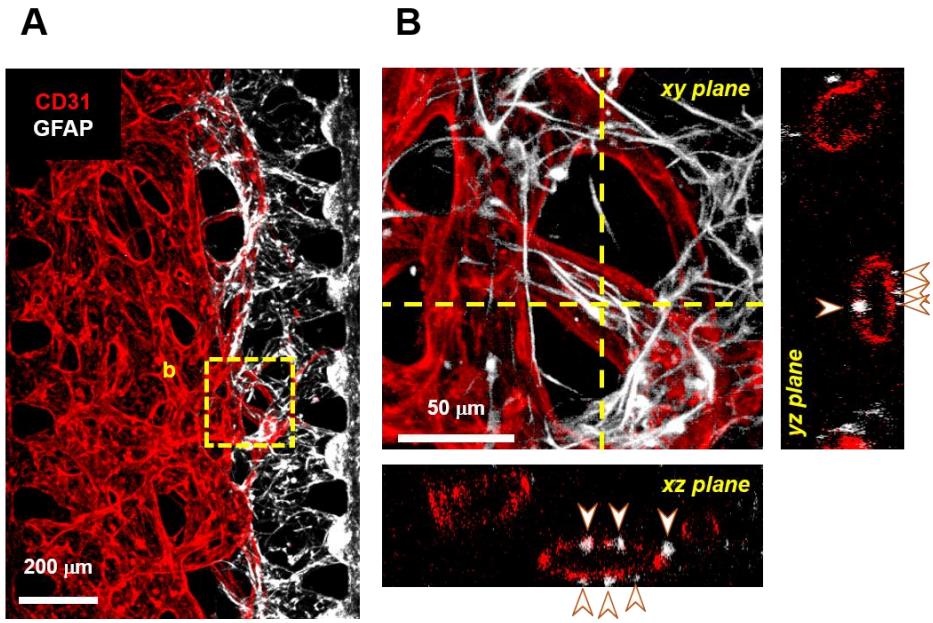

Figure 4-8. Direct contact of the vascular network and astrocytes. A large number of direct contacts between vascular network and astrocytes is observed not only xz plane but also yz plane (arrowhead).

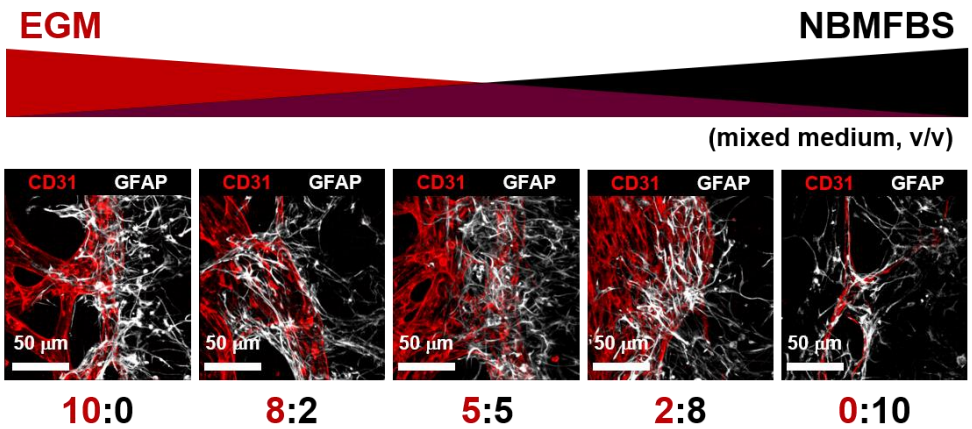

Figure 4-9. Direct contact between vascular network and astrocytes under various conditions. In this experiment, the medium in VC and NC is the same. Although medium conditions are different, a number of direct contacts occurs.

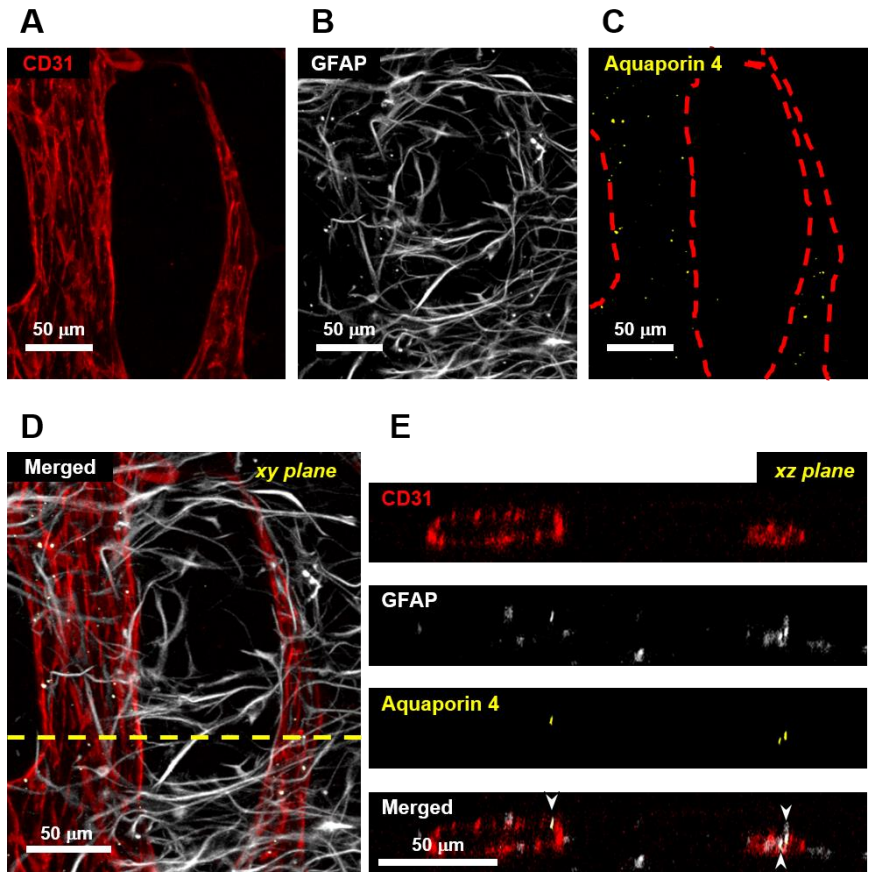

Figure 4-10. Expression of aquaporin 4 at the direct contact between vascular network and astrocytes. (A) Immunostained image of vascular network (B) Immunostained image of astrocytes (C) Immunostained image of aquaporin 4. The red dotted line represents the outline of the vascular network. The aquaporin 4 is mostly expressed on the vascular network. (D) Merged image of vascular network, astrocytes, and aquaporin 4. (E) The aquaporin 4 is expressed at the direct contact between vascular network and astrocytes.

4-3-3. The effect of medium in permeability

Permeability was quantified for flow exclusively through the lumen of the vascular network to the astrocytes. The vascular network was generated by means of seeding endothelial cells along the VNC. After the formation of the network, the space in between each micropost became the entry port of a single vascular lumen which stretched from post to post. (Fig. 4-11A and Fig. 12). Any substances introduced into the entrance of the vascular lumen would move into the vascular network through the lumen exclusively, and not through the fibrin hydrogel. As the formation of fully perfusable and closed lumen only occurred in co-cultures with EGM supplied VC, permeability tests could only be done on EGM supplied VC platforms. After introducing 20 kDa FITC-dextran into the vascular network via the VC, the amount of leakage outside of vascular network was measured in three conditions (medium in the VC/medium in the NC): only cultured vascular network (EGM/none) and co-cultured vascular network with different medium conditions (EGM/EGM and EGM/NBMFBS). Fluorescence in the vascular network was expressed immediately after introduction of FITC-dextran through the VC. The intensities of fluorescence inside and outside of vascular network were observed in real time (Fig. 11B). The permeability value of the

EGM/none condition was higher than that of EGM/EGM condition. In the case of the co-cultured platform, the permeability value of the EGM/NBMFBS condition was lower than that of EGM/EGM condition. (Permeability coefficients with 20 kDa FITC-dextran, EGM/none (n = 9), 1.85 ± 0.20 × 10^{-6} cm/s; EGM/EGM (n = 14), 0.65 ± 0.08 × 10^{-6} cm/s; EGM/NBMFBS (n = 13), 0.45 ± 0.11 × 10^{-6} cm/s; Permeability coefficients with 70 kDa FITC-dextran, EGM/none (n = 12), 1.39 ± 0.19 × 10^{-6} cm/s; EGM/EGM (n = 12), 0.60 ± 0.12 × 10^{-6} cm/s; EGM/NBMFBS (n = 20), 0.36 ± 0.05 × 10^{-6} cm/s (Fig. 11C and D). Comparison of permeability coefficients with other *in vitro* BBB models is summarized in Table 1.

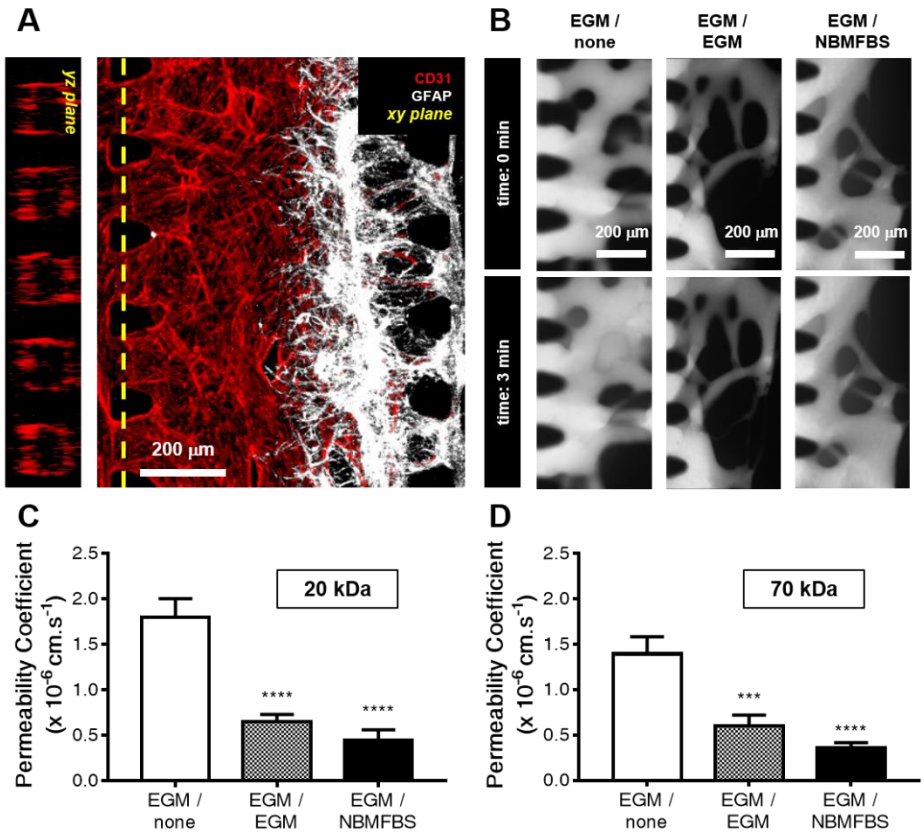
A
yz plane
CD31
GFAP
xy plane
200 µm
B
EGM / none
EGM / EGM
EGM / NBMFBS
time: 0 min
time: 3 min
200 µm
200 µm
200 µm
C
Permeability Coefficient (x 10-6 cm.s-1)
20 kDa
****
****
EGM / none
EGM / EGM
EGM / NBMFBS
D
Permeability Coefficient (x 10-6 cm.s-1)
70 kDa
***
****
EGM / none
EGM / EGM
EGM / NBMFBS

Figure 4-11. Vascular network - astrocyte complex permeability compared across the three experimental co-culture medium compositions. (A) Immunostained imaging of the vascular network and the astrocytic interface confirms that vascular lumens cover all of the areas between VC side microposts. This means that any substances introduced through the VC into the vascular network can be assumed to be flowing inside the vascular network and not in the fibrin hydrogel. (B) Time-lapse microscopic photographs at various medium conditions with 70 kDa FITC-dextran. (C) Results of permeability experiments with 20 kDa FITC-dextran. (D) Results of permeability experiments with 70 kDa FITC-dextran. All data show mean ± SEM. Statistical analysis student's t-test. ***$p < 0.001$, ****$p < 0.0001$.

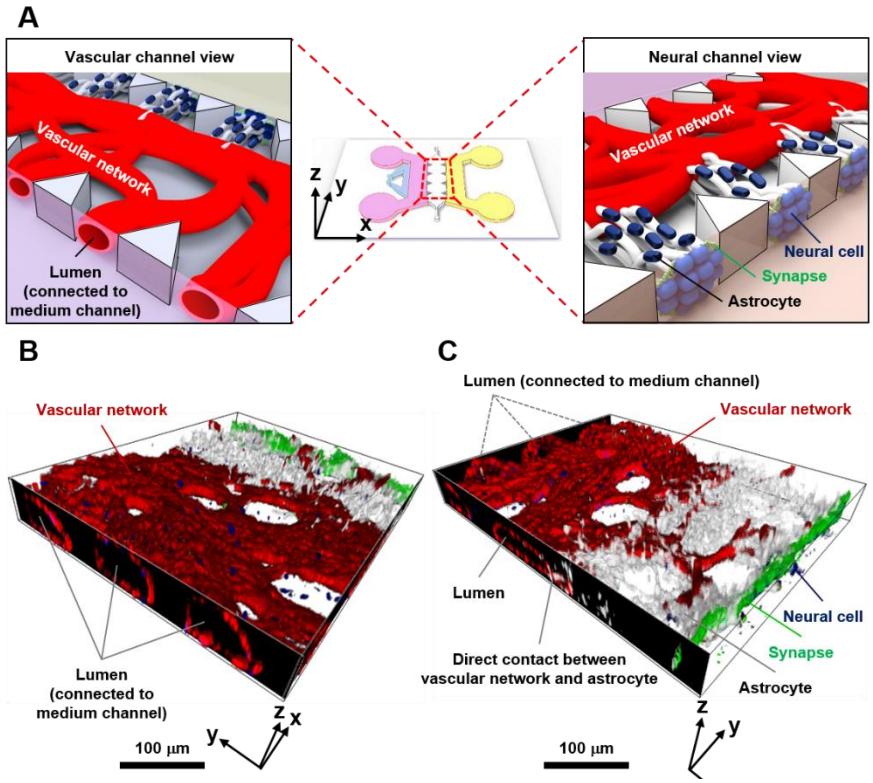

Figure 4-12. The 3D images of immunostained NVU platform. (A) Scheme of the microfluidic in vitro 3D NVU platform including BBB. (B) 3D NVU platform viewed from the direction of vascular channel. There is lumen between micro-posts that connects to the inside of the vascular network. (C) 3D NVU platform viewed from the direction of neural channel. Synapse is expressed at the area in contact with the neural channel. Also, as can be seen from the xz sectioned plane, the lumen of the vascular network is well maintained. These 3D images are reconstruction of figure 4-7.

Model	20 kDa (10^{-6} cm/s)	70 kDa (10^{-6} cm/s)	References
In vivo	0.24	0.15	Yuan, W. *et al.*[108]
Transwell	-	0.16	Li, G. *et al.* [105]
Microfluidic, membrane	~ 2	~ 0.7	Booth, R. *et al.* [92]
Microfluidic, hydrogel	-	~ 10	Adriani, G. *et al.* [97]
This work	0.45	0.36	

Table 4-1. Permeability coefficients in various in vitro BBB models measured by 20 kDa and 70 kDa FITCdextran.

4-4. Discussion

The blood-brain barrier, a critical part of the NVU, is formed from a three dimensional monolayer of endothelial cells directly interfaced with astrocytes via a system of capillaries and characterized by low permeability [81]. This study proposes a platform which is capable of generating a three dimensional BBB microfluidic platform which presents both structural and functional properties of the BBB *in vivo*. The vascular network generated in the proposed BBB platform is comprised of intact and perfusable monolayer capillaries and directly contacts astrocytes in a manner resembling the NVU [60].

Astrocytes, which are an important component of the BBB, plays a role in controlling capillary features and BBB permeability [105]. However, it is known that angiogenesis is inhibited if astrocytes and endothelial cells are plated at the same time [106]. Therefore, the cell plating procedure in this study emulated *in vivo* brain development in that blood vessels are generated before neuronal seeding [107].

In the neural cell culture of this study, the robust proliferation and the migration of astrocytes were rarely observed with exclusively NBMFBS supplied media, but observed in EGM supplied cultures (Fig. 4-2A). VEGF-A was also observed to promote the proliferation and the migration of

astrocytes (Fig. 4-3). In contrast, EGM/NBMFBS supplied co-cultures exhibited larger astrocytic areas than in EGM/EGM supplied co-cultures (Fig. 4-4C). The resulting data suggests that the gradient of VEGF-A in the fibrin hydrogel promotes astrocytes to proliferate and migrate toward the VC in EGM/NBMFBS supplied co-cultures. In EGM/EGM supplied co-cultures, the proliferation and the migration of astrocytes toward the VC are less pronounced due to the lack of VEGF-A gradient. Therefore, it was presumed that overlapped large area between vascular networks and astrocytes was made due to VEGF-A gradient within fibrin hydrogel at EGM/NBMFBS condition. The increase of the overlapped area between vascular network and astrocytes indicates that the total area of direct contact between vascular network and astrocytes is increased. It is known that vascular network expresses better BBB features when direct contact area between vascular network and astrocytes increases [106]. As a result, it could be assumed that the permeability at EGM/NBMFBS condition, which is similar to *in vivo* BBB, is lower than at EGM/EGM condition due to the increased direct contact area [108]. Consequently, it is reasonable that the permeability decreases as overlapped area between vascular network and astrocytes increases.

One limitation of this study is the use of umbilical cord endothelial cells

rather than brain derived endothelial cells. However, the study indicates that the platform can present structural and functional equivalency with *in vivo* BBB while still using HUVEC. Akiyama *et al*. also showed that HUVEC can be formed into the BBB when grafted into an *in vivo* mouse brain [109, 110]. Likewise, Hayashi *et al*. published that *in vitro* co-culture with astrocytes and HUVEC presents brain-type glucose transporter (GLUT-1) expression which is one of the characteristics of the BBB [106].

The NVU has many types of intercellular interactions, such as the interactions between endothelial cells and astrocytes, endothelial cells and microglia, and astrocytes and neurons [81, 114, 115]. The proposed platform cannot be called a complete NVU model as of yet, as it can only model the interactions between endothelial cells and astrocytes. Further studies are needed in order to expand the platform to an all-inclusive NVU on a chip, which would greatly accelerate the fields of neuroscience and neuropharmacology.

4-5. Summary

The proposed platform was designed to generate *in vitro* three dimensional co-culture tissues that emulate BBB form and function. In order to generate analogous *in vitro* microenvironmental conditions in both the vascular and neural locales, it was necessary to determine suitable media compositions with optimized quantities for each cell type utilized. Vascular-astrocytic contact areas and vascular network permeability were quantified as metrics to determine media suitability for *in vivo* like co-culture conditions.

Neuropharmacological research is severely hampered by BBB impermeability, as drugs must first pass the BBB before gaining access to the brain [111, 112, 113]. *In vivo*-like *in vitro* NVU platforms may promote research on brain disease models, and allow for an easier means of pharmacologically targeting the brain. Although the proposed co-culture method could be applied to other tissues co-cultured with naturally lumenized 3D vascular networks, the ultimate goal of this publication is to provide a complete *in vitro* NVU platform consisting of naturally lumenized 3D vascular networks, astrocytes with the BBB structure, and synapses on neurons.

Chapter 5. Conclusion

Neurons and glia cells in the brain have very elaborately complex structures. The two most important features of each of these structures are the neural circuit and the blood-brain barrier. In the brain, neural circuits are networked together to control the thinking and behavior of humans and animals. Because these networks are complexly interconnected, it is not easy to study and analyze a single neural circuit. Therefore, it is necessary to construct an independent neural circuit to study neural circuit easily. Neurons forming neural circuits in the brain are very weak beings. It is necessary to protect neurons, which are more sensitive to environmental changes than other cells forming the body, from external substances. Thus, there is a blood-brain barrier in the brain that blocks the diffusion of substances in the blood into the brain tissue. However, when drugs are needed in the brain tissue due to the presence of the blood-brain barrier, many new drugs are not actually applied. For this reason, it is necessary to develop a blood-brain barrier model.

In this thesis, we demonstrated engineering of mimicking two important structures of the brain, the neural circuit and the blood-brain barrier on the

microfluidic platform. Conventional *in vitro* cell culture methods enabled simple neuronal or vascular cell cultures, but they were very different from *in vivo* brain tissues due to very hard surfaces, randomly growing cells, and lack of 3D shapes such as lumen. The microfluidic platform using photolithography has been developed to decrease the size of constructs to the cell level and to resolve the disadvantages of existing in vitro cell culture. Therefore, the microfluidic technique enables the engineering of various *in vitro* cell culture methods.

First, we have designed a microfluidic platform to characterize axon growth of neurons. Through this, we found that the axon grows beyond the specific length and grows in the existing direction even at the intersection. This is an experiment that cannot be done because there is no guidance for the axon to grow straight in the conventional *in vitro* neuron culture. Based on these results, we could make a neuronal circuit of axon diode which is formed only in one direction, not bidirectional, when there are two neuron groups. However, it still had the drawback of 2D culture.

Second, we have devised a method for modifying the internal density pattern by applying pressure to the hydrogel after patterning the hydrogel on a microfluidic platform. When neurons are attached to one side of the deformed hydrogel, and then cultured, the axons grow into bundle shpae in the hydrogel. The axon bundle form is also observed in the *in vivo* nervous system. Furthermore, by positioning another neuron group at the end of the axon bundle, we could create a structurally and functionally intact 3D neural circuit.

Third, in order to mimic the blood-brain barrier, we had to co-culture the neural cell as well as the vascular network. However, the culture medium required for neural cells differs from the culture medium required for vascular networks. In order to provide different cultures to different cells, a vascular network that is only opened with one media channel inside the hydrogel was designed. After that, by placing neural cells on the side where the vascular network was not opened, cell culture media suitable for each cell could be provided. As a result, a structurally and functionally intact three-dimensional *in vitro* blood-brain barrier platform was created.

The results described in this thesis collectively indicate that we implemented cell patterning, hydrogel patterning, and pressure control that cannot be done in conventional *in vitro* cell culture by using microfluidics technology. The brain-on-a-chip is realized by fusing these functions with cell growth characteristics. We believe that the brain-on-a-chip can be used various applications such as high-throughput screening platform and platform for research of nervous system.

References

[1] Angevine, J.B., Bodian, D., Coulombre, A.J., Edds, M.V., Hamburger, V., Jacobson, M., Lyser, K.M., Prestige, M.C., Sidman, R.L., Varon, S., Weiss, P.A. Embryonic vertebrate central nervous system: revised terminology. *Anat Rec* **166**, 257-261 (1970).

[2] Herculano-Houzel, S. The human brain in numbers: a linearly scaled-up primate brain. *Front Hum Neurosci* **3**, 31 (2009).

[3] Weksler, B.B., Subileau, E.A., Perrière, N., Charneau, P., Holloway, K., Leveque, M., Tricoire-Leignel, H., Nicotra, A., Bourdoulous, S., Turowski, P., Male, D.K., Roux, F., Greenwood, J., Romero, I.A., Couraud, P.O. Blood-brain barrier-specific properties of a human adult brain endothelial cell line. *FASEB J* **19**, 1872-1874 (2005).

[4] Zolessi, F.R. Vertebrate neurogenesis: cell polarity. *encyclopedia of Life Sciences*, John Wiley & Sons, Chichester, 1-13 (2016).

[5] Livet, J., Weissman, T.A., Kang, H., Draft, R.W., Lu, J., Bennis, R. A., Sanes, J.R., Sanes Lichtman, J.W. Transgenic strategies for combinatorial expression of fluorescent proteins in the nervous system. *Nature* **450**, 56-62 (2007).

[6] Pardridge, W.M. The blood-brain barrier: bottleneck in brain drug development. *Neurotherapeutics* **2**, 3-14 (2005).

[7] Huttenlocher, P.R. Synaptic density in human frontal cortex-developmental changes and effects of aging. *Brain Res* **163**, 195-205 (1979).

[8] Kennedy, T.E., Serafini, T., de la Torre, J. R., Tessier-Lavigne, M. Netrins are diffusible chemotropic factors for commissural axons in the embryonic spinal cord. *Cell* **78**, 425-435 (1994).

[9] Yuan, W., Zhou, L., Chen, J.-H., Wu, J.Y., Rao, Y., Ornitz, D.M. The mouse slit family: secreted ligands for ROBO expressed in patterns that suggest a role in morphogenesis and axon guidance. *Dev Biol* **212**, 290-306 (1999).

[10] Koser, D.E., Thompson, A.J., Foster, S.K., Dwivedy, A., Pillai, E.K., Sheridan, G.K., Svoboda, H., Viana, M., Costa, L.D., Guck, J., Holt, C.E., Franze, K. Mechanosensing is critical for axon growth in the developing brain. *Nat Neurosci* **19**, 1592-1598 (2016).

[11] Chen, Z.Y., Sun, C., Reuhl, K., Bergemann, A., Henkemeyer, M., Zhou, R. Abnormal hippocampal axon bundling in EphB receptor mutant mice. *J Neurosci* **24**, 2366-2374 (2004).

[12] Banks, W.A. From blood–brain barrier to blood–brain interface: new opportunities for CNS drug delivery. *Nat Rev Drug Discov* **15**, 275-292 (2016).

[13] Bhatia, S.N., Ingber, D.E. Microfluidic organs-on-chips. *Nature Biotech* **32**,760-772 (2014).

[14] Na, S., Kang, M., Bang, S., Park, D., Kim, J., Sim, S.J., Chang, S., Jeon, N.L. *Technology* **4**, 240-248 (2016).

[15] Peters, A., Kaiserman-Abramof, I.R. The small pyramidal neuron of the rat cerebral cortex. the perikaryon, dendrites and spines. *Am J Anat* **127**, 321–355 (1970).

[16] Williams, R.W., Herrup, K. The control of neuron number. *Annu Rev Neurosci* **11**, 423–453 (1988).

[17] Bean, B.P. The action potential in mammalian central neurons. *Nat Rev Neurosci* **8**, 451–465 (2007).

[18] Getting, P.A. Emerging principles governing the operation of neural networks. *Annu Rev Neurosci* **12**, 185–204 (1989).

[19] Hormuzdi, S.G., Filippov, M.A., Mitropoulou, G., Monyer, H., Bruzzone, R. Electrical synapses: a dynamic signaling system that shapes the activity of neuronal networks. *Biochim Biophys Acta* **1662**, 113–137 (2004).

[20] Renault, R., Durand, J.-B., Viovy, J.-L., Villard, C. Asymmetric axonal edge guidance: a new paradigm for building oriented neuronal networks. *Lab Chip* **16**, 2188–2191 (2016).

[21] le Feber, J., Postma, W., de Weerd, E., Weusthof, M., Rutten, W.L. Barbed channels enhance unidirectional connectivity between neuronal networks cultured on multi electrode arrays. *Front Neurosci* **9**, 412 (2015).

[22] Chang, C., Glover, G.H. Time-frequency dynamics of resting-state brain connectivity measured with fMRI. *Neuroimage* **50**, 81–98 (2010).

[23] van den Heuvel, M.P., Hulshoff Pol, H.E. Exploring the brain network: a review on resting-state fMRI functional connectivity. *Eur Neuropsychopharmacol* **20**, 519–534 (2010).

[24] Ray, J., Peterson, D.A., Schinstine, M., Gage, F.H. Proliferation, differentiation, and longterm culture of primary hippocampal neurons. *Proc Nat Acad Sci* **90**, 3602–3606 (1993).

[25] Marom, S., Shahaf, G. Development, learning and memory in large random networks of cortical neurons: lessons beyond anatomy. *Q Rev Biophys* **35**, 63–87 (2002).

[26] Li, L., Yang, Y., Shi, X., Wu, H., Chen, H., Liu, J. A microfluidic system for the study of the response of endothelial cells under pressure. *Microfluid Nanofluid* **16**, 1089–1096 (2014).

[27] Hansen, A.S., Hao, N., O'Shea, E.K. High-throughput microfluidics to control and measure signaling dynamics in single yeast cells. *Nat Protoc* **10**, 1181–1197 (2015).

[28] Dura, B., Dougan, S.K., Barisa, M., Hoehl, M.M., Lo, C.T., Ploegh, H.L.,

Voldman, J. Profiling lymphocyte interactions at the single-cell level by microfluidic cell pairing. *Nat Commun* **6**, 5940 (2015).

[29] Destexhe, A., Contreras, D., Steriade, M., Sejnowski, T.J., Huguenard, J.R. In vivo, in vitro, and computational analysis of dendritic calcium currents in thalamic reticular neurons. *J Neurosci* **16**, 169–185 (1996).

[30] Bang, S., Na, S., Jang, J.M., Kim, J., Jeon, N.L. Engineering-aligned 3D neural circuit in microfluidic device. *Adv Healthc Mater* **5**, 159–166 (2016).

[31] Helmstaedter, M., Briggman, K.L., Turaga, S.C., Jain, V., Seung, H.S., Denk, W. Connectomic reconstruction of the inner plexiform layer in the mouse retina. *Nature* **500**, 168–174 (2013).

[32] Park, J.W., Kim, H.J., Kang, M.W., Jeon, N.L. Advances in microfluidics-based experimental methods for neuroscience research. *Lab Chip* **13**, 509–521 (2013).

[33] Silva, G.A. Neuroscience nanotechnology: Progress, opportunities and challenges. *Nat Rev Neurosci* **7**, 65–74 (2006).

[34] Taylor, A.M., Blurton-Jones, M., Rhee, S.W., Cribbs, D.H., Cotman, C.W., Jeon, N.L. A microfluidic culture platform for CNS axonal injury, regeneration and transport. *Nat Methods* **2**, 599–605 (2005).

[35] Takeuchi, A., Nakafutami, S., Tani, H., Mori, M., Takayama, Y., Moriguchi, H., Kotani, K., Miwa, K., Lee, J.K., Noshiro, M., Jimbo, Y. Device for co-culture of sympathetic neurons and cardiomyocytes using microfabrication. *Lab Chip* **11**, 2268–2275 (2011).

[36] Peyrin, J.M., Deleglise, B., Saias, L, Vignes, M., Gougis, P., Magnifico, S., Betuing, S., Pietri, M., Caboche, J., Vanhoutte, P., Viovy, J.L., Brugg, B. Axon diodes for the reconstruction of oriented neuronal networks in microfluidic chambers. *Lab Chip* **11**, 3663–3673 (2011).

[37] Honegger, T., Scott, M.A., Yanik, M.F., Voldman, J. Electrokinetic

confinement of axonal growth for dynamically configurable neural networks. *Lab Chip* **13**, 589–598 (2013).

[38] Feinerman, O., Rotem, A., Moses, E. Reliable neuronal logic devices from patterned hippocampal cultures. *Nat Phys* **4**, 967–973 (2008).

[39] Grieger, J.C., Choi, V.W., Samulski, R.J. Production and characterization of adenoassociated viral vectors. *Nat Protoc* **1**, 1412–1428 (2006).

[40] Song, H.J., Ming, G.L., Poo, M.M. cAMP-induced switching in turning direction of nerve growth cones. *Nature* **388**, 275–279 (1997).

[41] Li, N., Folch, A. Integration of topographical and biochemical cues by axons during growth on microfabricated 3-D substrates. *Exp Cell Res* **311**, 307–316 (2005).

[42] Tesla, N. (U.S. Patent No. 1,329,559, 3 February 1920).

[43] Taylor, A.M., Rhee, S.W., Tu, C.H., Cribbs, D.H., Cotman, C.W., Jeon, N.L. Microfluidic multicompartment device for neuroscience research. *Langmuir* **19**, 1551–1556 (2003).

[44] Morin, F., Nishimura, N., Griscom, L., Lepioufle, B., Fujita, H., Takamura, Y., Tamiya, E. Constraining the connectivity of neuronal networks cultured on microelectrode arrays with microfluidic techniques: a step towards neuron-based functional chips. *Biosens Bioelectron* **21**, 1093–1100 (2006).

[45] Allen, T.G. Preparation and maintenance of single-cell micro-island cultures of basal forebrain neurons. *Nat Protoc* **1**, 2543–2550 (2006).

[46] Gil, V., del Rio, J.A. Analysis of axonal growth and cell migration in 3D hydrogel cultures of embryonic mouse CNS tissue. *Nat Protoc* **7**, 268–280 (2012).

[47] Tomba, C., Braini, C., Wu, B., Gov, N.S., Villard, C. Tuning the adhesive geometry of neurons: Length and polarity control. *Soft Matter* **10**, 2381–2387

(2014).
[48] Suter, D.M., Forscher, P. Substrate-cytoskeletal coupling as a mechanism for the regulation of growth cone motility and guidance. *J Neurobiol* **44**, 97–113 (2000).
[49] Lowery, L.A., Van Vactor, D. The trip of the tip: Understanding the growth cone machinery. *Nat Rev Mol Cell Biol* **10**, 332–343 (2009).
[50] Petrie, R.J., Gavara, N., Chadwick, R.S., Yamada, K.M. Nonpolarized signaling reveals two distinct modes of 3D cell migration. *J Cell Biol* **197**, 439-455 (2012).
[51] Kramer, N., Walzl, A., Unger, C., Rosner, M., Krupitza, G., Hengstschläger, M., Dolznig, H. In vitro cell migration and invasion assays. *Mutation Res/Rev Mutation Res* **752**, 10-24 (2013).
[52] Lee, S.J., Atala, A. Scaffold technologies for controlling cell behavior in tissue engineering Scaffold technologies for controlling cell behavior in tissue engineering. *Biomed Mater* **8**, 1-2 (2013).
[53] Watt, F.M., Huck, W.T. Role of the extracellular matrix in regulating stem cell fate. *Nat Rev Mol Cell Biol* **14**, 467-473 (2013).
[54] Pautot, S., Wyart, C., Isacoff, E.Y. Colloid-guided assembly of oriented 3D neuronal networks. *Nat Methods* **5**, 735-740 (2008).
[55] Tang-Schomer, M.D., White, J.D., Tien L.W., Schmitt, L.I., Valentin, T.M., Graziana, D.J., Hopkins, A.M., Omenetto, F.G., Haydon, P.G., Kaplan, D.L. Bioengineered functional brain-like cortical tissue. *Proc Nat Acad Sci* **111**, 13811–13816 (2014).
[56] Yang, F., Murugan, R., Wang, S., Ramakrishna, S. Electrospinning of nano/micro scale poly(L-lactic acid) aligned fibers and their potential in neural tissue engineering. *Biomaterials* **26**, 2603-2610 (2005).
[57] Papadopoulou, E.L., Samara, A., Barberoglou, M., Manousaki, A.,

Pagakis, S.N., Anastasiadou, E., Fotakis, C., Stratakis, E. Silicon scaffolds promoting three-dimensional neuronal web of cytoplasmic processes. *Tissue Eng Part C* **16**, 497-502 (2009).

[58] Huh, D., Hamilton, G.A., Ingber, D.E. From 3D cell culture to organs-on-chips. *Trends Cell Biol* **21**, 745-754 (2011).

[59] Sung, J.H., Yu, J., Luo, D., Shuler, M.L., March, J.C. Microscale 3-D hydrogel scaffold for biomimetic gastrointestinal (GI) tract model. *Lab Chip* **11**, 389-392 (2011).

[60] Kim, S., Lee, H., Chung, M., Jeon, N.L. Engineering of functional, perfusable 3D microvascular networks on a chip. *Lab Chip* **13**, 1489-1500 (2013).

[61] Yamada, M., Utoh, R., Ohashi, K., Tatsumi, K., Yamato, M., Okano, T., Seki, M. Controlled formation of heterotypic hepatic micro-organoids in anisotropic hydrogel microfibers for long-term preservation of liver-specific functions. *Biomaterials* **33**, 8304-8315 (2012).

[62] Hume, S.L., Hoyt, S.M., Walker, J.S., Sridhar, B.V., Ashley, J.F., Bowman, C.N., Bryant, S.J. Alignment of multi-layered muscle cells within three-dimensional hydrogel macrochannels. *Acta Biomater* **8**, 2193-2202 (2012).

[63] Hoffman, A.S. Hydrogels for biomedical applications. *Adv Drug Del Rev* **64**, 18-23 (2012).

[64] Verhulsel, M., Vignes, M., Descroix, S., Malaquin, L., Vignjevic, D.M., Viovy, J.L. A review of microfabrication and hydrogel engineering for micro-organs on chips. Biomaterials 35, 1816-1832 (2014).

[65] Ribeiro, A., Vargo, S., Powell, E.M., Leach, J.B. Substrate three-dimensionality induces elemental morphological transformation of sensory

neurons on a physiologic timescale. *Tissue Eng Part A* **18**, 93-102 (2012).

[66] Lampe, K.J., Mooney, R.G., Bjugstad, K.B., Mahoney, M.J. Effect of macromer weight percent on neural cell growth in 2D and 3D nondegradable PEG hydrogel culture. *J Biomed Mater Res Part A* **94A**, 1162-1171 (2010).

[67] Fawcett, J.W., Barker, R.A., Dunnett, S.B. Dopaminergic neuronal survival and the effects of bFGF in explant, three dimensional and monolayer cultures of embryonic rat ventral mesencephalon. *Exp Brain Res* **106**, 275-282 (1995).

[68] Horie, H., Akahori, Y. Three-dimensional cell aggregation enhances growth-promoting activity of NGF in adult DRG. *Neuroreport* **30**, 37-40 (1994).

[69] Pardo, B., Honegger, P. Differentiation of rat striatal embryonic stem cells in vitro: monolayer culture vs. three-dimensional coculture with differentiated brain cells. *J Neurosci Res* **59**, 504-512 (2000).

[70] Kunze, A., Giugliano, M., Valero, A., Renaud, P. Micropatterning neural cell cultures in 3D with a multi-layered scaffold. *Biomaterials* **32**, 2088-2098 (2011).

[71] Odawara, A., Gotoh, M., Suzuki, I. Control of neural network patterning using collagen gel photothermal etching. *Lab Chip* **13**, 2040-2046 (2013).

[72] Kothapalli, C.R., van Veen, E., de Valence, S., Chung, S., Zervantonakis, I.K., Gertler, F.B., Kamm, R.D. A high-throughput microfluidic assay to study neurite response to growth factor gradients. *Lab Chip* **11**, 497-507 (2011).

[73] Van Vactor D. Adhesion and signaling in axonal fasciculation. *Curr Opin*

Neurobiol **8**, 80-86 (1988).

[74] Hopkins, A.M., DeSimone, E., Chwalek, K., Kaplan, D.L. 3D in vitro modeling of the central nervous system. *Prog Neurobiol* **125**, 1-25 (2015).

[75] Odawara, A., Gotoh, M., Suzuki, I. A three-dimensional neuronal culture technique that controls the direction of neurite elongation and the position of soma to mimic the layered structure of the brain. *RSC Adv* **3**, 23620-23630 (2013).

[76] Jang, J.M., Tran, S.H.T., Na, S.C., Jeon, N.L. Engineering controllable architecture in matrigel for 3d cell alignment. *ACS Appl Mater Interf* **7**, 2183-2188 (2015).

[77] Huang, C.P., Lu, J., Seon, H., Lee, A.P., Flanagan, L.A., Kim, H.Y., Putnam, A.J., Jeon, N.L. Engineering microscale cellular niches for three-dimensional multicellular co-cultures. *Lab Chip* **9**, 1740-1748 (2009).

[78] Bang, S., Lee, S.R., Ko, J., Son, K., Tahk, D., Ahn, J., Im, C., Jeon, N.L. A low permeability microfluidic blood-brain barrier platform with direct contact between perfusable vascular network and astrocytes. *Sci Rep* **7**, 8083 (2017).

[79] Hawkins, B. T., Davis, T. P. The blood-brain barrier/neurovascular unit in health and disease. *Pharmacol Rev* **57**, 173–185 (2005).

[80] Muoio, V., Persson, P. B., Sendeski, M. M. The neurovascular unit – concept review. *Acta Physiol* **210**, 790–798 (2014).

[81] Abbott, N. J., Ronnback, L., Hansson, E. Astrocyte-endothelial interactions at the blood-brain barrier. *Nat Rev Neurosci* **7**, 41–53 (2006).

[82] Rajkowska, G., Hughes, J., Stockmeier, C. A., Javier Miguel-Hidalgo, J., Maciag, D. Coverage of blood vessels by astrocytic endfeet is reduced in

major depressive disorder. *Biol Psychiatry* **73**, 613–621 (2013).

[83] Nielsen, S., Nagelhus, E.A., Amiry-Moghaddam, M., Bourque, C., Agre, P., Ottersen, O.P. Specialized membrane domains for water transport in glial cells: high-resolution immunogold cytochemistry of aquaporin-4 in rat brain. *J Neurosci* **17**, 171–180 (1997).

[84] Abbott, N. J. Inflammatory mediators and modulation of blood–brain barrier permeability. *Cell Mol Neurobiol* **20**, 131–147 (2000).

[85] Schinkel, A.H., Smit, J.J., van Tellingen, O., Beijnen, J.H., Wagenaar, E., van Deemter, L., Mol, C.A., van der Valk, M.A., Robanus-Maandag, E.C., te Riele, H.P., Berns, A.J.M., Borst, P. Disruption of the mouse mdr1a P-glycoprotein gene leads to a deficiency in the blood-brain barrier and to increased sensitivity to drugs. *Cell* **77**, 491–502 (1994).

[86] Cecchelli, R., Berezowski, V., Lundquist, S., Culot, M., Renftel, M., Dehouck, M.P., Fenart, L. Modelling of the blood–brain barrier in drug discovery and development. *Nat Rev Drug Discov* **6**, 650–661 (2007).

[87] Hatherell, K., Couraud, P.-O., Romero, I. A., Weksler, B., Pilkington, G. J. Development of a three-dimensional, all-human in vitro model of the blood–brain barrier using mono-, co-, and tri-cultivation Transwell models. *J Neurosci Methods* **199**, 223–229 (2011).

[88] Naik, P., Cucullo, L. In vitro blood–brain barrier models: current and perspective technologies. *J Pharm Sci* **101**, 1337–1354 (2012).

[89] Pardridge, W. M., Triguero, D., Yang, J., Cancilla, P. A. Comparison of in vitro and in vivo models of drug transcytosis through the blood-brain barrier. *J Pharmacol Exp Ther* **253**, 884–891 (1990).

[90] Rubin, L.L., Hall, D.E., Porter, S., Barbu, K., Cannon, C., Horner, H.C., Janatpour, M., Liaw, C.W., Manning, K., Morales, J. A cell culture model of the blood-brain barrier. *J Cell Biol* **115**, 1725–1735 (1991).

[91] Achyuta, A.K., Conway, A.J., Crouse, R.B., Bannister, E.C., Lee, R.N., Katnik, C.P., Behensky, A.A., Cuevas, J., Sundaram, S.S. A modular approach to create a neurovascular unit-on-a-chip. *Lab Chip* **13**, 542–553 (2013).

[92] Booth, R., Kim, H. Characterization of a microfluidic in vitro model of the blood-brain barrier (μBBB). *Lab Chip* **12**, 1784–1792 (2012).

[93] Brown, J.A., Pensabene, V., Markov, D.A., Allwardt, V., Neely, M.D., Shi, M., Britt, C.M., Hoilett, O.S., Yang, Q., Brewer, B.M., Samson, P.C., McCawley, L.J., May, J.M., Webb, D.J., Li, D., Bowman, A.B., Reiserer, R.S., Wikswo, J.P. Recreating blood-brain barrier physiology and structure on chip: A novel neurovascular microfluidic bioreactor. *Biomicrofluidics* **9**, 054124 (2015).

[94] Walter, F. R., Valkai, S., Kincses, A., Petneházi, A., Czeller, T., Veszelka, S., Ormos, P., Deli, M.A., Dér, A. A versatile lab-on-a-chip tool for modeling biological barriers. *Sensors and Actuators B* **222**, 1209–1219 (2016).

[95] Chiu, D. T., Jeon, N.L., Huang, S., Kane, R.S., Wargo, C.J., Choi, I.S., Ingber, D.E., Whitesides, G.M. Patterned deposition of cells and proteins onto surfaces by using three-dimensional microfluidic systems. *Proc Nat Acad Sci* **97**, 2408–2413 (2000).

[96] Kim, S., Kim, H. J., Jeon, N. L. Biological applications of microfluidic gradient devices. *Integr Biol* **2**, 584–603 (2010).

[97] Adriani, G., Ma, D. L., Pavesi, A., Kamm, R., Goh, E.L.K. A 3D neurovascular microfluidic model consisting of neurons, astrocytes and cerebral endothelial cells as blood-brain barrier. *Lab Chip* **17**, 448–459 (2017).

[98] Xu, H., Li, Z., Yu, Y., Sizdahkhani, S., Ho, W.S., Yin, F., Wang, L., Zhu, G., Zhang, M., Jiang, L., Zhuang, Z., Qin, J. A dynamic in vivo-like organotypic blood-brain barrier model to probe metastatic brain tumors. *Sci Rep* **6**, 36670 (2016).

[99] Kim, J., Chung, M., Kim, S., Jo, D.H., Kim, J.H., Jeon, N.L. Engineering of a biomimetic pericyte-covered 3D microvascular network. *PloS One* **10**, e0133880 (2015).

[100] Choi, Y. J., Park, J., Lee, S.-H. Size-controllable networked neurospheres as a 3D neuronal tissue model for Alzheimer's disease studies. *Biomaterials* **34**, 2938–2946 (2013).

[101] Cullen, D. K., Gilroy, M. E., Irons, H. R., LaPlaca, M. C. Synapse-to-neuron ratio is inversely related to neuronal density in mature neuronal cultures. *Brain Res* **1359**, 44–55 (2010).

[102] Mani, N., Khaibullina, A., Krum, J. M., Rosenstein, J. M. Astrocyte growth effects of vascular endothelial growth factor (VEGF) application to perinatal neocortical explants: receptor mediation and signal transduction pathways. *Exp Neurol* **192**, 394–406 (2005).

[103] Wuestefeld, R., Chen, J., Meller, K., Brand-Saberi, B., Theiss, C. Impact of VEGF on astrocytes: analysis of gap junctional intercellular communication, proliferation, and motility. *Glia* **60**, 936–947 (2012).

[104] Stevenson, B. R., Siliciano, J. D., Mooseker, M. S., Goodenough, D. A. Identification of ZO-1: a high molecular weight polypeptide associated with the tight junction (zonula occludens) in a variety of epithelia. *J Cell Biol* **103**, 755–766 (1986).

[105] Li, G., Simon, M.J., Cancel, L.M., Shi, Z.D., Ji, X., Tarbell, J.M., Morrison, B., Fu, B.M. Permeability of endothelial and astrocyte cocultures: in vitro blood–brain barrier models for drug delivery studies. *Ann Biomed Eng* **38**, 2499–2511 (2010).

[106] Hayashi, Y., Nomura, M., Yamagishi, S., Harada, S., Yamashita, J., Yamamoto, H. Induction of various blood-brain barrier properties in non-neural endothelial cells by close apposition to co-cultured astrocytes. *Glia* **19**,

13–26 (1997).

[107] Zerlin, M., Goldman, J. E. Interactions between glial progenitors and blood vessels during early postnatal corticogenesis: blood vessel contact represents an early stage of astrocyte differentiation. *J Comp Neurol* **387**, 537–546 (1997).

[108] Yuan, W., Lv, Y., Zeng, M., Fu, B.M. Non-invasive measurement of solute permeability in cerebral microvessels of the rat. *Microvasc Res* **77**, 166–173 (2009).

[109] Akiyama, H., Kondoh, T., Kokunai, T., Nagashima, T., Saito, N., Tamaki, N. Blood-brain barrier formation of grafted human umbilical vein endothelial cells in athymic mouse brain. *Brain Res* **858**, 172–176 (2000).

[110] Wu, C.C., Chen, Y.C., Chang, Y.C., Wang, L.W., Lin, Y.C., Chiang, Y.L., Ho, C.J., Huang, C.C. Human umbilical vein endothelial cells protect against hypoxic-ischemic damage in neonatal brain via stromal cell derived factor 1/CXC chemokine receptor type 4. *Stroke* **44**, 1402–1409 (2013).

[111] Kola, I., Landis, J. Can the pharmaceutical industry reduce attrition rates? *Nat Rev Drug Discov* **3**, 711–716 (2004).

[112] Pangalos, M. N., Schechter, L. E., Hurko, O. Drug development for CNS disorders: strategies for balancing risk and reducing attrition. *Nat Rev Drug Discov* **6**, 521–532 (2007).

[113] Pardridge, W. M. The blood-brain barrier: bottleneck in brain drug development. *NeuroRx* **2**, 3–14 (2005).

[114] Dudvarski Stankovic, N., Teodorczyk, M., Ploen, R., Zipp, F., Schmidt, M.H.H. Microglia–blood vessel interactions: a doubleedged sword in brain pathologies. *Acta Neuropathol* **131**, 347–363 (2016).

[115] Banerjee, S., Bhat, M. A. Neuron-Glial Interactions in Blood-Brain Barrier Formation. *Annu Rev Neurosci* **30**, 235–258 (2007).

국문초록

본 학위 논문에서는 복잡한 두뇌 조직을 미세유체 플랫폼에서 다양한 방식으로 모사하는 것을 목적으로 하였다. 실제의 두뇌 조직은 너무나 복잡하여 여전히 완전히 밝혀지지 않았다. 사람 두뇌의 경우, 1000 억개의 신경 세포와 신경 세포 개수의 10 배 이상의 교세포가 정교하게 정렬되어 기능을 수행한다. 이렇게 복잡한 두뇌 조직 중 대표적인 두 가지 구조는 신경 회로와 혈액-뇌 장벽이다. 신경 회로의 특징은 한 쪽으로 정렬된 축삭 돌기들에 의하여 신호가 단방향성으로 전달된다는 것이다. 혈액-뇌 장벽의 특징은 교세포의 한 종류인 성상세포가 혈관에 접촉하여 혈관의 투과성을 매우 낮춘다는 것이다. 기존의 생체 외 세포 배양 방식은 페트리 접시 혹은 커버 슬립과 같은 단순한 2 차원 환경에서 이루어져 실제 두뇌의 환경과는 큰 차이가 있었다. 이러한 한계를 극복하기 위하여 미세유체 플랫폼을 이용하여 세포 크기 수준의 채널 디자인, 압력을 이용한 하이드로젤의 구조 변형, 두 종류 이상의 세포 공배양을 위한

채널 디자인 등을 제어함으로써 실제 두뇌 조직을 모사한 생체 외 배양 플랫폼을 제작할 수 있다.

먼저, 세포 크기 수준의 채널의 형상이 신경 세포의 축삭 돌기 생장에 미치는 영향을 알아보았다. 신경 세포는 신호를 전달하기 위하여 다수의 짧은 수상 돌기로부터 신호를 받고 이를 하나의 긴 축삭 돌기로 전달한다. 길고 얇은 형태를 갖는 축삭 돌기가 자라는 특성을 알아보기 위하여 신경 세포의 부위 중 축삭 돌기만 지날 수 있는 미세 채널을 제작하였다. 미세 채널의 디자인은 축삭 돌기가 특정 길이의 직선만큼 생장한 후 나오는 갈림길에서 어느 방향으로 생장하는지 확인할 수 있도록 제작되었다. 그 결과 축삭 돌기는 120 μm 이상 직진하여 생장하면 이후의 생장에 있어 해당 방향으로 직진성을 갖는 것을 확인하였다. 이러한 축삭 돌기 생장 특징을 이용하여 고리 형태가 연속된 미세 채널을 디자인한 결과 분리된 두 개의 신경 세포 그룹 간에 한 방향으로만 축삭 돌기가 연결되는 단방향성의 신경 회로가 구축됨을 확인하였다.

다음으로는 미세유체 플랫폼에서 패터닝 된 하이드로젤을 압력으로 내부 밀도 패턴을 변화시킨 후 이 하이드로젤이 신경

세포 축삭 돌기 생장에 미치는 영향을 알아보았다. 100 μm 크기의 미세 기둥들이 100 μm 간격으로 촘촘히 세워진 미세 기둥 배열을 3 줄 이상 나란히 위치시킨 디자인의 미세유체 플랫폼에 생체 하이드로젤의 일종인 마트리젤을 패터닝한 후, 미디어 채널을 통하여 마트리젤의 한 쪽 면에만 약 12 mm 높이의 수압을 가하였다. 이러한 비대칭 압력을 3 시간 이상 가하게 되면 마트리젤이 미세 기둥들 사이로 밀려나오게 된다. 그 후 마트리젤의 양 면에 동일한 양의 세포 배양액을 위치시켜 마트리젤이 변형된 상태로 안정화되도록 하였을 때, 변형된 마트리젤의 내부 밀도는 등방성으로 균일하지 않고 규칙적으로 밀한 영역과 소한 영역으로 내부 밀도가 패터닝된다. 이러한 마트리젤의 한 쪽 면에 신경 세포를 부착하여 배양한 결과 신경 세포의 축삭 돌기들이 마트리젤의 밀도가 소한 영역으로 모여 번들 형태를 형성함을 확인하였다. 이러한 번들 형태의 축삭 돌기 모임은 실제 두뇌의 신경 회로에서도 관찰된다. 미세유체 플랫폼의 디자인을 변형하여 축삭 돌기 모임 말단 부분에 새로운 신경 세포 그룹을 위치시킴으로써 구조적, 기능적으로 두뇌의

신경 회로와 유사한 생체 외 3 차원 신경 회로가 구축됨을 확인하였다.

마지막으로 미세유체 플랫폼 내에서 공배양되는 두 종류 이상의 세포에 적합한 세포 배양액을 독립적으로 제공할 수 있는 방법이 공배양에 미치는 영향을 알아보았다. 미세유체 플랫폼에서 혈관 세포와 신경 세포와의 공배양 환경을 이루기 위하여 두 세포를 처음부터 함께 키우기보다 혈관 세포 먼저 안정적으로 배양을 시작하였다. 이 시기에는 혈관 세포 배양액만을 사용한다. 미세유체 플랫폼에 두 세포 배양액 채널 사이에 패턴된 하이드로젤 내부에서 혈관 세포가 혈관 네트워크를 이루기 시작할 무렵에 신경 세포를 하이드로젤 한 쪽 벽면에 부착한다. 이 시기부터는 신경 세포 쪽 채널에는 신경 세포 배양액을, 반대편 채널에는 혈관 세포 배양액을 사용한다. 이후 5 일 이상 배양하면 혈관 네트워크의 루멘이 혈관 세포 배양액 쪽 채널로만 열리게 된다. 즉, 혈관 네트워크 내부로는 혈관 세포 배양액이, 신경 세포로는 신경 세포 배양액이 독립적으로 제공된다. 이러한 공배양 조건에서 배양한 결과, 두뇌 조직의 혈액-뇌 장벽에서

보이는 성상 세포가 혈관에 닿아있는 형태적 특징 및 혈관의 낮은 투과성을 모두 구축됨을 확인하였다.

위의 결과들에서 볼 수 있듯이 신경 세포는 미세유체 플랫폼의 채널 형태 및 하이드로젤의 변형된 형태에 민감하게 반응한다. 우리는 이러한 물리적 요소 혹은 기계적 요소를 사용하여 신경 세포의 생장 형태를 제어할 수 있었다. 또한 다양한 세포 간의 공배양을 위하여 각 세포 종류에 맞는 세포 배양액을 제공할 수 있는 방법을 개발한 결과 다양한 세포 종류 간의 상호 작용을 관찰할 수 있었다. 신경 세포의 구조와 기능을 정밀하게 제어할 수 있는 미세유체 플랫폼을 이용하여 형성한 브레인-온-어-칩은 기초 뇌과학 연구용 플랫폼 및 약물 스크리닝 플랫폼 등 다양한 분야에 적용될 수 있을 것이다.

주요어: 미세유체 플랫폼, 신경 세포, 신경 회로, 축삭 돌기 다이오드, 축삭 돌기 다발, 혈액-뇌 장벽, 세포 공배양

학번: 2012-22556